iScience

CellPress
OPEN ACCESS

Article

BDNF-dependent nano-organization of Neogenin and the WAVE regulatory complex promotes actin remodeling in dendritic spines

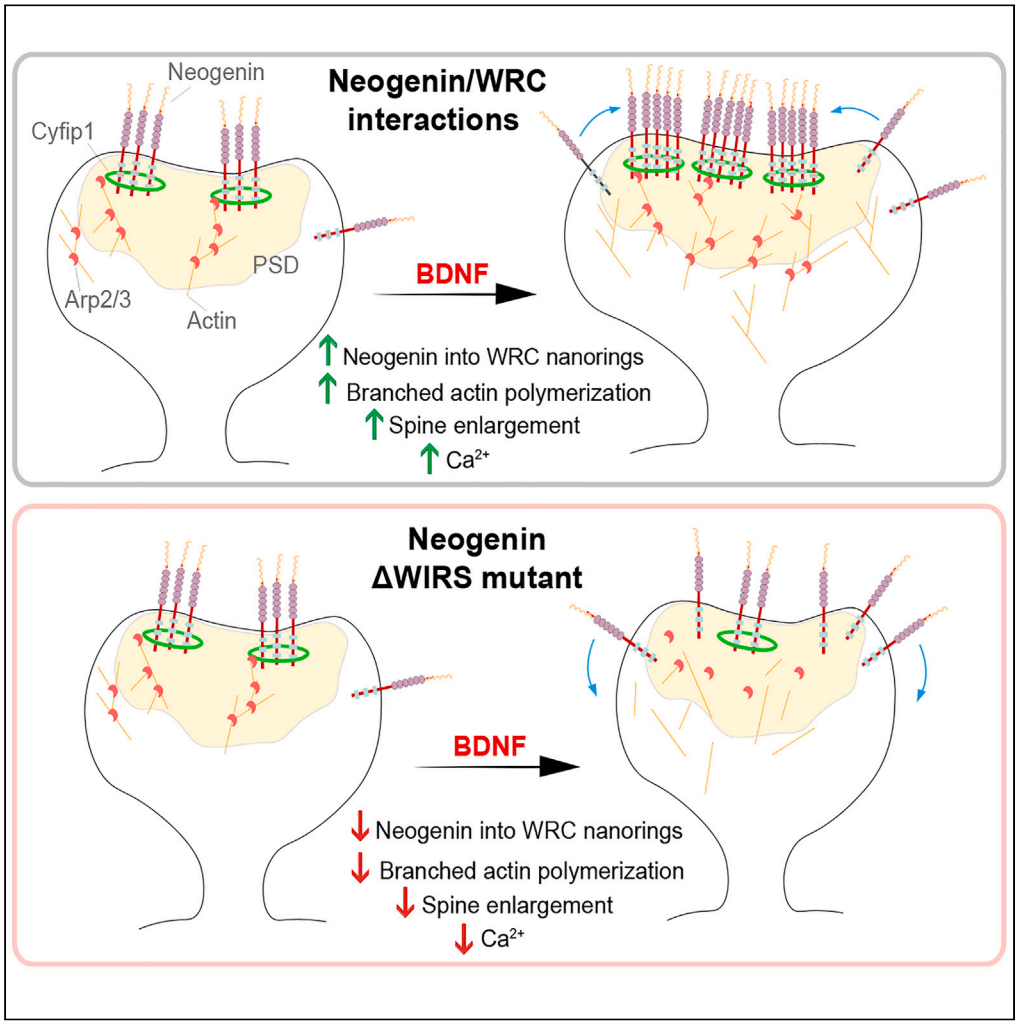

Belal Shohayeb, Kai Sempert, Tristan P. Wallis, ..., Elizabeth A. O'Brien, Cecilia Flores, Helen M. Cooper

h.cooper@uq.edu.au

Highlights

Neogenin is highly organized on the dendritic spine membrane at the nanoscale level

BDNF induces Neogenin/WRC coclustering into nanodomains at the postsynaptic density

Disruption of Neogenin/WRC binding blocks BDNF-mediated actin remodeling in spines

Inhibiting Neogenin/WRC binding prevents BDNF-induced calcium signaling in spines

Shohayeb et al., iScience 27, 110621
September 20, 2024
https://doi.org/10.1016/j.isci.2024.110621

iScience

CellPress
OPEN ACCESS

Article

BDNF-dependent nano-organization of Neogenin and the WAVE regulatory complex promotes actin remodeling in dendritic spines

Belal Shohayeb,[1] Kai Sempert,[1] Tristan P. Wallis,[1,2] Frédéric A. Meunier,[1,2,3] Nela Durisic,[1] Elizabeth A. O'Brien,[1] Cecilia Flores,[4,5,6] and Helen M. Cooper[1,7,*]

SUMMARY

Synaptic structural plasticity, the expansion of dendritic spines in response to synaptic stimulation, is essential for experience-dependent plasticity and is driven by branched actin polymerization. The WAVE regulatory complex (WRC) is confined to nanodomains at the postsynaptic membrane where it catalyzes actin polymerization. As the netrin/RGM receptor Neogenin is a critical regulator of the WRC, its nanoscale organization may be an important determinant of WRC nanoarchitecture and function. Using super-resolution microscopy, we reveal that Neogenin is highly organized on the spine membrane at the nanoscale level. We show that Neogenin binding to the WRC promotes co-clustering into nanodomains in response to brain-derived neurotrophic factor (BDNF), indicating that nanoclustering occurs in response to synaptic stimulation. Disruption of Neogenin/WRC binding not only prevents BDNF-mediated actin remodeling but also inhibits BDNF-induced calcium signaling. We conclude that the assembly of Neogenin/WRC nanodomains is a prerequisite for BDNF-mediated structural and synaptic plasticity.

INTRODUCTION

Synaptic structural plasticity, the ability of the dendritic spine to undergo morphological changes in response to synaptic stimulation is an essential determinant of synaptic strength.[1–5] Actin remodeling is the driving force for spine enlargement during spinogenesis and experience-dependent plasticity.[4,6–10] During the induction of long-term potentiation (LTP), the cellular correlate of learning and memory, actin synthesis rapidly increases spine volume independent of protein synthesis, whereas LTP consolidation requires actin polymerization and mRNA translation.[8,9,11] Brain-derived neurotrophic factor (BDNF) is a pivotal regulator of structural and functional synaptic plasticity and is released from both the pre- and postsynaptic compartments of excitatory synapses in response to synaptic activation.[1,12–15] Sustained BDNF signaling via the TrkB receptor is necessary for LTP induction and maintenance as it activates multiple signaling pathways and promotes actin remodeling.[1,12,14,16–18] Currently, however, we have little insight into the factors that control actin regulators in the spine, especially with respect to those acting downstream of BDNF.

The dynamic actin pool is situated adjacent to the postsynaptic density (PSD) and comprises a dense network of branched actin which seeds F-actin growth. The Arp2/3 enzymatic complex, an inefficient actin nucleator, catalyzes branched actin polymerization and is activated by the pentameric WAVE regulatory complex (WRC).[19–23] In spines, the WRC subunit Cyfip1 also acts as a translational repressor where it binds the translation initiation factor, EIF4E, and the fragile X protein (FMRP) preventing translation of FMRP-bound mRNAs.[16,24–26] BDNF reinforces synaptic strength by ensuring that actin polymerization and protein synthesis are spatiotemporally coordinated. In the early phase of LTP, BDNF promotes protein synthesis in an activity-dependent manner by initiating the dissociation of Cyfip1 from the EIF4E-FMRP complex thereby relieving translational repression.[16,24–26] The subsequent incorporation of Cyfip1 into the WRC facilitates actin remodeling.

With the advent of super-resolution microscopy, it is now clear that the nanoscale organization of ion channel subunits and signaling molecules at the PSD is dynamically regulated. The nanoscale alignment of presynaptic glutamate release sites with postsynaptic ion channels (trans-synaptic nanocolumns) is believed to underly efficient synaptic transmission.[27–30] It is not surprising then that tight spatiotemporal control of postsynaptic actin regulators at the nanoscale level is also required for efficient actin remodeling and spine enlargement.[8,31] The WRC is confined within nanodomains overlapping the PSD in close apposition to Arp2/3[31] and recent studies in lamellipodia indicate that diffusion

[1]Queensland Brain Institute, The University of Queensland, Brisbane, QLD 4072, Australia
[2]Clem Jones Centre for Ageing Dementia Research, Queensland Brain Institute, The University of Queensland, Brisbane, QLD 4072, Australia
[3]The School of Biomedical Sciences, The University of Queensland, Brisbane, QLD 4072, Australia
[4]Department of Psychiatry and Department of Neurology and Neurosurgery, McGill University, Montréal, Canada
[5]Douglas Mental Health University Institute, Montréal, Canada
[6]Ludmer Centre for Neuroinformatics & Mental Health, McGill University, Montréal, Canada
[7]Lead contact
*Correspondence: h.cooper@uq.edu.au
https://doi.org/10.1016/j.isci.2024.110621

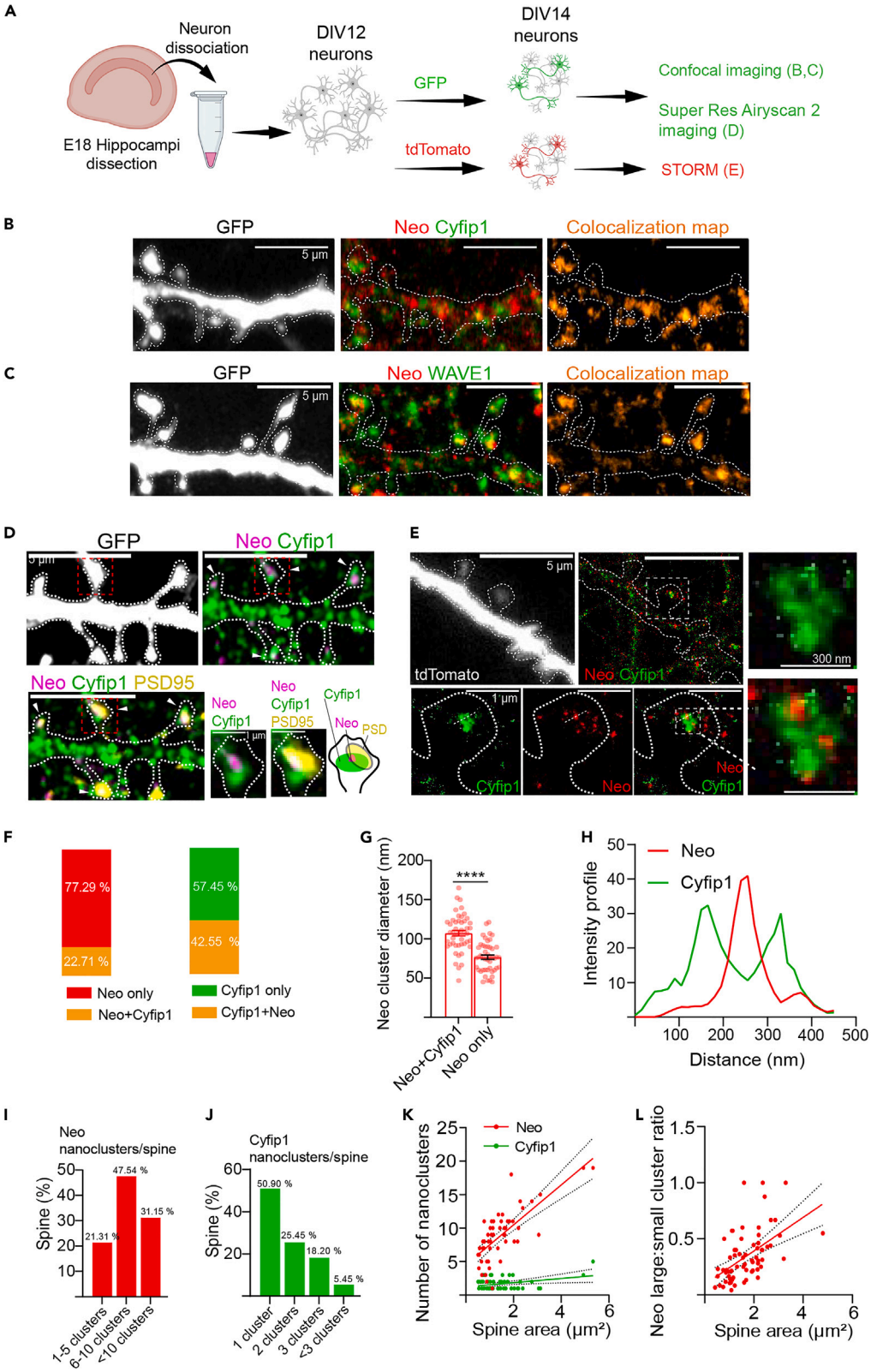
A
Neuron dissociation
DIV12 neurons
DIV14 neurons
E18 Hippocampi dissection
GFP
tdTomato
Confocal imaging (B,C)
Super Res Airyscan 2 imaging (D)
STORM (E)
B
GFP
Neo Cyfip1
Colocalization map
5 µm
C
GFP
Neo WAVE1
Colocalization map
5 µm
D
GFP
Neo Cyfip1
Neo Cyfip1 PSD95
Neo Cyfip1
Neo Cyfip1 PSD95
Cyfip1
Neo PSD
E
5 µm
tdTomato
Neo Cyfip1
300 nm
1 µm
Cyfip1
Neo
Neo Cyfip1
F
77.29 %
22.71 %
57.45 %
42.55 %
Neo only
Neo+Cyfip1
Cyfip1 only
Cyfip1+Neo
G
Neo cluster diameter (nm)
****
Neo+Cyfip1
Neo only
H
Neo
Cyfip1
Intensity profile
Distance (nm)
I
Neo nanoclusters/spine
Spine (%)
47.54 %
31.15 %
21.31 %
1-5 clusters
6-10 clusters
>10 clusters
J
Cyfip1 nanoclusters/spine
Spine (%)
50.90 %
25.45 %
18.20 %
5.45 %
1 cluster
2 clusters
3 clusters
>3 clusters
K
Neo
Cyfip1
Number of nanoclusters
Spine area (µm²)
L
Neo large:small cluster ratio
Spine area (µm²)

Figure 1. Neogenin forms nanoclusters with the WRC on dendritic spines

(A) Schematic outlines the experimental workflow.

(B and C) Endogenous Neogenin colocalizes with the WRC subunits Cyfip1 (B) and WAVE1 (C) on spines of hippocampal neurons expressing GFP.

(D) Super-resolution confocal microscopy (90 nm resolution) shows that Neogenin and Cyfip1 colocalize with the PSD protein PSD-95.

(E) STORM imaging (20 nm resolution): Neogenin is clustered within Cyfip1 nanodomains and also forms nanoclusters independently of Cyfip1.

(F) Percentage of Neogenin associated with Cyfip1 nanodomains (N = 53 spines) and percentage of Cyfip1 nanoclusters associated with Neogenin (N = 55 spines).

(G) Quantification of Neogenin/Cyfip1 and Neogenin-only nanocluster diameters (unpaired Student's t test, $p < 0.0001$, F(46, 46) = 1.516; $p = 0.1620$, N = 47 spines, mean ± SEM, ****$p < 0.0001$).

(H) Line-scan analysis of fluorescence intensities shows that Neogenin is surrounded by a ring of Cyfip1.

(I and J) Percentage of Neogenin (N = 61 spines) or Cyfip1 nanoclusters (N = 55 spines) per spine.

(K) Pearson correlation analysis of Neogenin nanoclusters/spine (red, $R^2 = 0.55$, slope = 2.38 ± 0.30, F(1, 50) = 61.11, $p < 0.0001$) and Cyfip1 nanoclusters/spine (green, $R^2 = 0.12$, slope = 0.25 ± 0.09, F(1, 50) = 6.484, $p = 0.0141$) correlates with increasing spine size (N = 52 spines).

(L) Pearson correlation analysis of Neogenin cluster size with increasing spine size ($R^2 = 0.28$, slope = 0.17 ± 0.03, F(1, 65) = 25.34, $p < 0.0001$, N = 67 spines). Also see Figures S1 and S2.

trapping of the WRC into nanoscale rings is required for optimal Arp2/3 activation.[32,33] Although many WRC interactors have been identified in the postsynaptic compartment, the molecular mechanisms responsible for the recruitment of the WRC into these structures, especially in the context of synaptic stimulation, are poorly understood. We propose that the Netrin/RGMa (Repulsive Guidance Molecule Receptor a), Neogenin, is an important determinant of WRC nanoscale distribution and function.

Neogenin plays a central role in cortical development[34–40] and is now emerging as a critical component of the excitatory postsynaptic apparatus regulating synaptic plasticity. Neogenin is essential for the induction and maintenance of LTP in the pyramidal neurons of the amygdala and hippocampus and in dentate gyrus granule cell synapses.[41,42] Recently, we identified a pivotal role for Neogenin in promoting spine enlargement.[43] We demonstrated that Neogenin binding to the WRC via its cytoplasmic WRC interacting receptor sequence (WIRS) facilitates Arp2/3-dependent branched actin polymerization.[43] This observation suggests that the coordinated sequestration of Neogenin and the WRC into nanoclusters at the PSD may be an important regulatory mechanism driving structural plasticity. However, the mechanisms governing Neogenin and WRC nanoscale organization and behavior on the postsynaptic membrane in response to synaptic stimulation have not been explored. We now test the hypothesis that BDNF-mediated synaptic stimulation promotes the partitioning of Neogenin and the WRC into nanoscale structures, thereby ensuring efficient actin polymerization at the PSD.

RESULTS

Neogenin forms nanoclusters with the WRC on dendritic spines

To investigate the spatial relationship between Neogenin and the WRC on spines, cultured excitatory hippocampal neurons from day 18.5 mouse embryos were transfected with GFP at day 12 *in vitro* (DIV12) (Figures 1A and S1A). Neurons were then fixed at DIV14 and immunolabelled for Neogenin, Cyfip1 and WAVE1. Neogenin and the WRC subunits were found to be concentrated in spines and were also present on the dendritic shaft (Figures 1B, 1C, and S1B). Colocalization maps revealed extensive overlap between Neogenin and both Cyfip1 and WAVE1 in spine heads and high-resolution confocal microscopy (90 nm resolution, Figure 1D) demonstrated that Cyfip1 and Neogenin were tightly associated with the PSD marker, PSD-95. Super-resolution stochastic optical reconstruction microscopy (STORM) imaging of spines (20 nm resolution, Figure 1E) further revealed that Neogenin exists on the spine membrane in two distinct nanostructures. Seventy-seven percent of nanoclusters had a mean diameter of 60 nm and contained several Neogenin molecules per cluster (Figures 1F, 1G, S1C, and S1D). The remaining 23% of clusters (mean diameter 100 nm) were enclosed within larger Cyfip1 nanodomains (Figures 1E–1G and S1E). Line-scan analysis of fluorescence intensities confirmed that Neogenin clusters were surrounded by a ring of Cyfip1 with a mean diameter of 182 nm (distance between Cyfip1 intensity peaks, Figure 1H). This is in line with previous studies reporting that the WRC subunits Abi1 and Nckap1 form 122–248 nm nanodomains at the PSD and that the WRC forms 230 nm ring-like structures in lamellipodia.[31,32] In addition, a second population of Cyfip1 nanodomains (57%) was not associated with Neogenin (Figure 1F). Although the number of Neogenin clusters per spine varied, 47% of spines contained 6–10 Neogenin clusters (Figure 1I). In contrast, the majority of spines contained only one Cyfip1 cluster (Figure 1J). Furthermore, the number of Neogenin nanoclusters increased with increasing spine size (Figure 1K). There was also a significant but weaker correlation between Cyfip1 cluster number and spine size. We also observed that the ratio of larger (≥ 100 nm) to smaller Neogenin nanoclusters (<100 nm) scaled with increasing spine size (Figure 1L). These observations correlate well with previous studies reporting that most spines contain one to four PSD-95 nanodomains and that the number of nanodomains scales with spine size.[27,44,45] Together these findings establish that Neogenin is highly organized at the nanoscale level where a subpopulation of receptors is tethered within WRC nanodomains on the spine membrane.

The WIRS motif found in the Neogenin cytoplasmic domain binds to the highly conserved Cyfip1/Abi1 surface which forms only when the WRC is fully assembled.[19,35,46] To demonstrate that the Neogenin-WRC interaction takes place on the spine, we employed the proximity ligation assay (PLA), an antibody-based assay that detects protein-protein interactions represented by fluorescent puncta. We transfected cDNAs encoding Neogenin (Neo) or NeoΔWIRS carrying mutations in the WIRS motif (Figure S2A) into DIV12 hippocampal neurons and performed the assay two days later. We observed no significant difference in the levels of Neo or NeoΔWIRS expression in spines (Figure S2B). A 2.6-fold decrease in the frequency of Neogenin/Cyfip1 puncta was observed for NeoΔWIRS compared to wildtype Neo (Figure S2C), confirming that the Neogenin WIRS motif binds the WRC in spines.

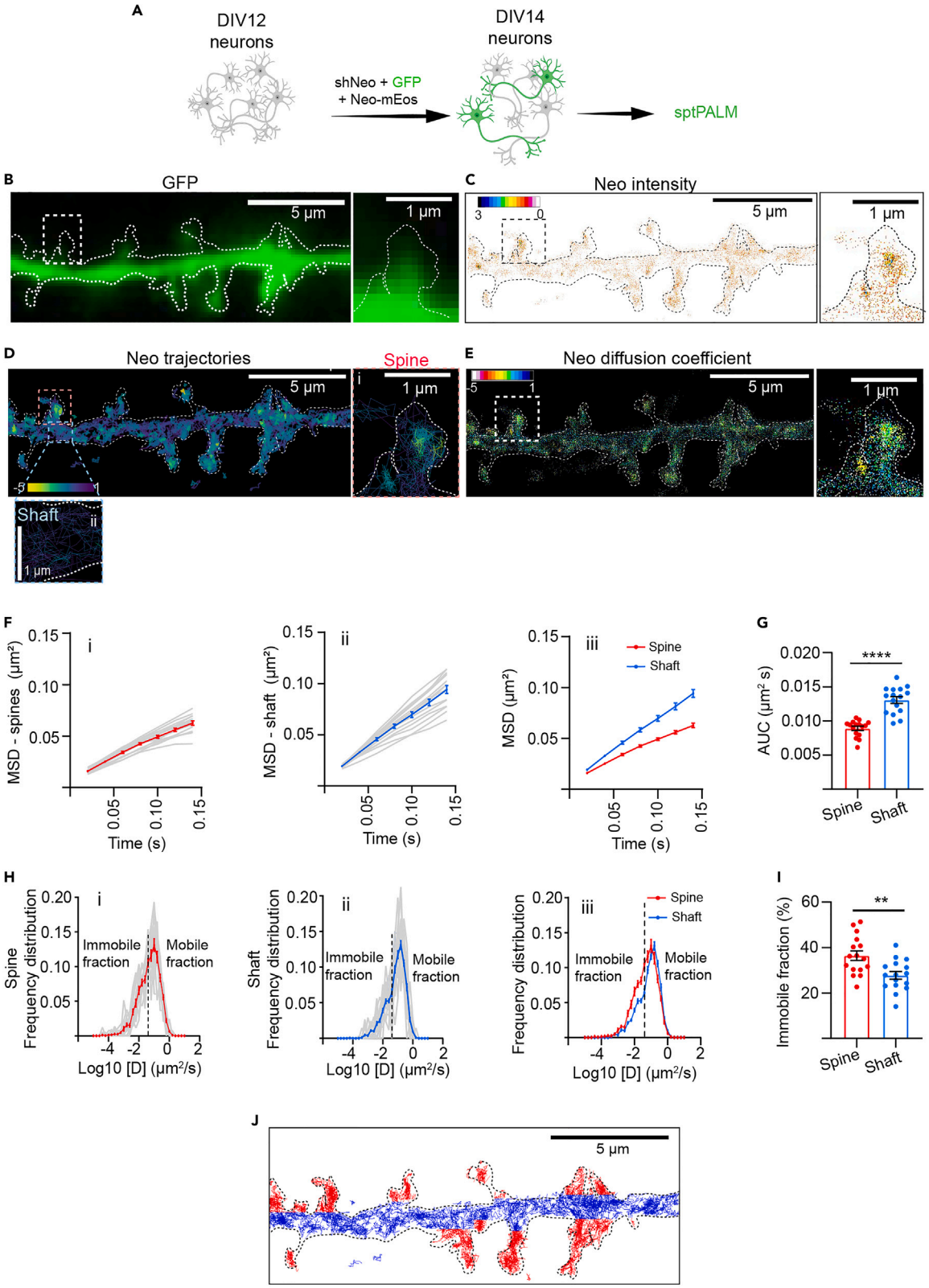
A
DIV12 neurons
shNeo + GFP + Neo-mEos
DIV14 neurons
sptPALM
B
GFP
5 µm
1 µm
C
Neo intensity
3
0
5 µm
1 µm
D
Neo trajectories
Spine
i
5 µm
1 µm
-5
1
Shaft
ii
1 µm
E
Neo diffusion coefficient
-5
1
5 µm
1 µm
F
i
ii
iii
MSD - spines (µm²)
MSD - shaft (µm²)
MSD (µm²)
Spine
Shaft
Time (s)
G
AUC (µm² s)
****
Spine
Shaft
H
i
ii
iii
Spine Frequency distribution
Shaft Frequency distribution
Frequency distribution
Immobile fraction
Mobile fraction
Log10 [D] (µm²/s)
I
Immobile fraction (%)
**
Spine
Shaft
J
5 µm

Figure 2. Neogenin mobility is confined within spines compared to shafts

(A) Schematic outlines the experimental workflow.

(B) Representative image of GFP epifluorescence in hippocampal neurons cotransfected with Neo shRNA and Neo-mEos.

(C–E) (C) Neo-mEos localization intensity map (blue, higher localization intensity), (D) map of individual trajectories, and (E) diffusion coefficient map (blue, higher mobility).

(F) Average mean squared displacement as a function of time for Neo-mEos trajectories calculated for (i) spines (red = mean) or (ii) shafts (blue = mean) and (iii) mean squared displacement for shafts versus spines.

(G) Neo-mEos mobility (Area Under the Curve, AUC) is reduced for spines compared to shafts.

(H) Frequency distribution curves for Neo-mEos diffusion coefficients [D] calculated for (i) spines (mean = red) or (ii) shafts (mean = blue) and (iii) mean diffusion coefficient frequency distribution for shafts versus spines. Dotted line: threshold value (−1.45 $\mu m^2/s$) segregating immobile and mobile fractions.

(I) Neo-mEos immobile fraction is increased in spines compared to shafts. (F and H) Gray lines represent single neurons. Unpaired Student's t test; (G) $p < 0.0001$; $F(15, 15) = 2.683$, $p = 0.0652$, (I) $p = 0.0031$; $F(15, 15) = 1.547$, $p = 0.407$. (G and I) $N = 16$ neurons, mean ± SEM, $^{**}p < 0.01$, $^{****}p < 0.0001$.

(J) Neo-mEos trajectories on the spine membrane (red) are more confined compared to the shaft (blue). Also see Figure S3.

Neogenin mobility is restricted in dendritic spines compared to shafts

The aforementioned data demonstrate that Neogenin molecules are confined within nanoclusters on the spine membrane where 23% are associated with Cyfip1 nanodomains. We therefore turned to single-particle tracking photoactivated localization microscopy (sptPALM)[47] to investigate the nanoscale dynamics of Neogenin on the shaft and spine membrane of live hippocampal neurons. We employed an RNA interference approach that efficiently inhibits Neogenin/WRC-mediated spine enlargement.[43] Neogenin specific shRNA (shNeo) but not the control shRNA (shCtl) reduced Neogenin expression in HEK293T cells by greater than 80% whereas RNAi-resistant Neogenin (fused at the C-terminus to mEos3.1, Neo-mEos) and NeoΔWIRS-mEos were not affected (Figures S3A and S3B). We have previously reported a 50% reduction in Neogenin after shNeo knockdown.[43] During spine morphogenesis thin spines convert to mature mushroom spines[4,48–50]— a process dependent on Neogenin/WRC-mediated branched actin polymerization.[43] To demonstrate that loss of Neogenin prevents spine enlargement hippocampal neurons were transfected with Neo-mEos and shNeo or shCtl at DIV12. Spine size was then assessed at DIV14. As previously shown,[43] shRNA depletion of Neogenin resulted in a 52% reduction in mature mushroom spines whereas Neo-mEos restored the number of mushroom spines to control levels (Figures S3C and S3D), demonstrating that the Neo-mEos fusion protein is fully functional.

To assess Neogenin nanoscale mobility on spines and shafts neurons were cotransfected at DIV12 with GFP, shNeo, and Neo-mEos (Figure 2A). At DIV14 Neo-mEos was stochastically photoconverted from green to red using 405 nm illumination at low spatial density and photoconverted molecules were tracked using a 561 nm laser. Sequences of sparsely photoconverted molecules were acquired at 50 Hz for 500 s (25,000 frames) which allowed the localization and tracking of single trajectories on individual spines and shafts. In agreement with our STORM imaging, super-resolved single-molecule localization intensity and trajectory maps (Figures 2B–2D) revealed that Neo-mEos trajectories were localized to clustered domains on the spine whereas Neo-mEos was more diffusely distributed throughout the dendritic shaft. To compare the extent of Neo-mEos lateral diffusion the average mean squared displacement of Neo-mEos trajectories on the plasma membrane was calculated (Figure 2F). The area under the curve was then used to statistically compare the mean squared displacements (Figure 2G). This analysis revealed that the mobility of Neo-mEos molecules was reduced by 31.8% in spines relative to shafts. The frequency distribution of the diffusion coefficients from all neurons was also calculated and a spatial map of the diffusion coefficients generated in PALM-Tracer (Figure 2E). The mean distribution of Neo-mEos between the mobile and immobile fractions was then determined from the Log_{10}diffusion coefficient threshold (−1.45 $\mu m^2/s$)[51] (Figure 2H). A significant shift to the left was observed for the spine frequency distribution curve relative to that for shafts, indicating that Neo-mEos diffusivity was reduced in spines compared to shafts. In addition, a 1.3-fold increase in the proportion of Neo-mEos molecules confined to the immobile fraction was seen in spines relative to shafts (36.5% versus 27.8% respectively, Figure 2I). Therefore, our data indicate that Neogenin lateral diffusion is markedly reduced on the spine membrane compared to the dendritic shaft (Figure 2J).

BDNF induces WRC-dependent Neogenin nanoclustering in spines

BDNF increases Cyfip1 availability in the spine and thus WRC formation at the PSD.[24,25] As Neogenin co-clusters with Cyfip1 in the spine head, we next determined whether BDNF promotes the incorporation of Neogenin and Cyfip1 into the PSD. High-resolution confocal colocalization maps (Figures 3A–3C) revealed that the addition of BDNF to neuronal cultures resulted in a 27% increase in the number of endogenous Neogenin and Cyfip1 clusters associated with the PSD-95 domain (Figures 3D and 3E). This suggests that BDNF regulates the nanoarchitecture of Neogenin and the WRC at the PSD.

To investigate whether Neogenin nanoscale dynamics is influenced by BDNF sptPALM was performed on hippocampal spines after shRNA depletion of Neogenin (Figure 4A). We also investigated whether Neogenin incorporation into WRC nanodomains was dependent on its interaction with the WRC by rescuing with either Neo-mEos or NeoΔWIRS-Eos. Super-resolved single-molecule localization intensity, trajectory and diffusion coefficient maps were generated (Figures 4B–4E) and the mean squared displacement (Figure 4F), the area under the curve (mobility, Figure 4G) and the immobile fraction (Figure 4H) derived for each. The addition of BDNF promoted a 19% decrease in mobility (Figures 4F and 4G) and a 27% increase in the immobilized fraction (Figure 4H) of Neo-mEos above control levels but had no effect on NeoΔWIRS-mEos mobility, indicating that BDNF enhances the confinement of Neogenin on the spine membrane in a WRC-dependent manner. WRC-mediated diffusion trapping of Neogenin also occurred in the absence of BDNF, albeit with reduced efficacy. Relative to Neo-mEos, a significant 1.2-fold increase in NeoΔWIRS-mEos mobility (Figures 4F and 4G) coupled with a non-significant reduction (16%) in the immobile

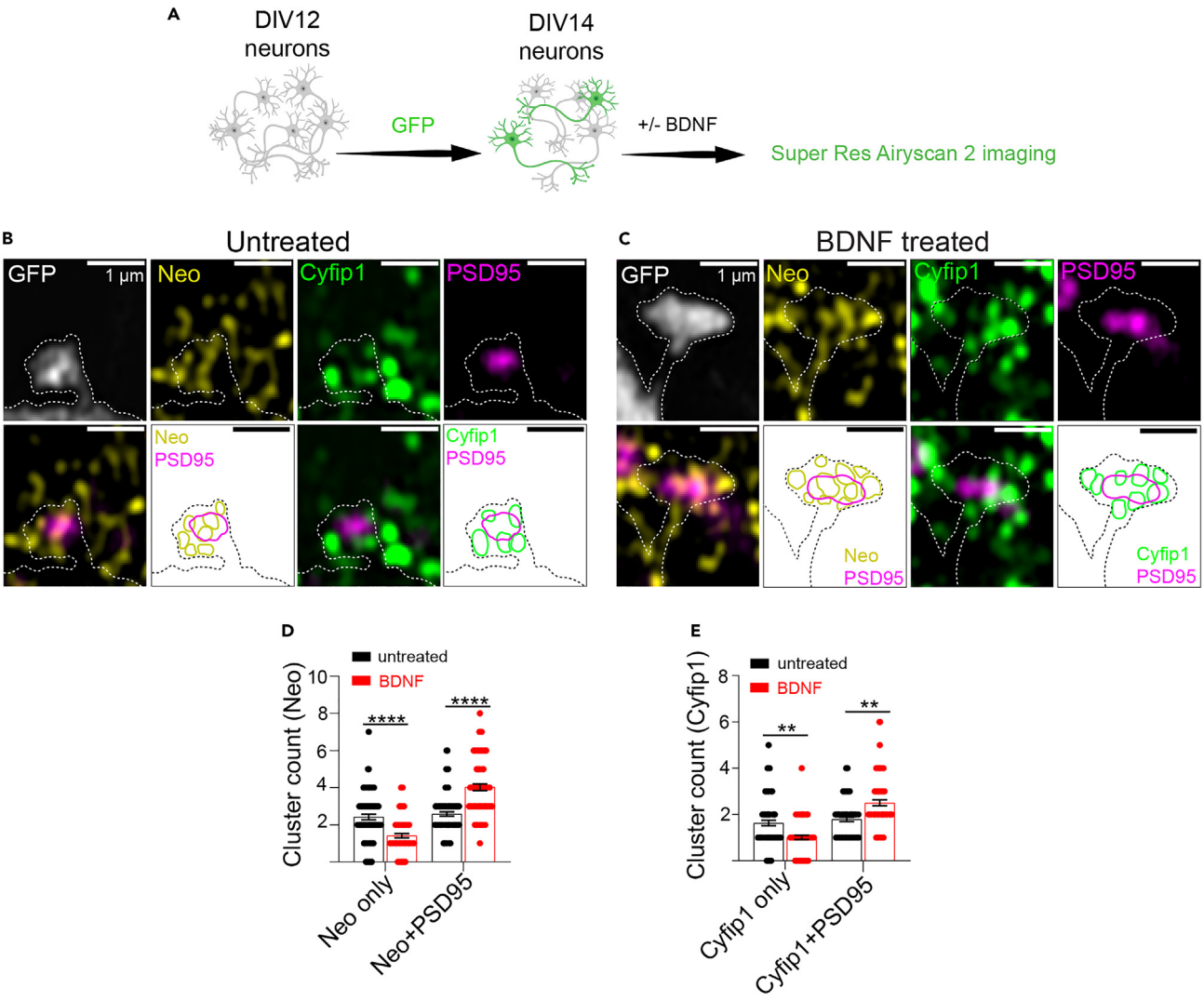

Figure 3. BDNF increases Neogenin/Cyfip1 association with the postsynaptic density

(A) Immunolabelling was performed in hippocampal neurons expressing GFP before and after BDNF treatment. Images were captured using the super-resolution Airyscan 2 microscope.

(B and C) Representative images of GFP (gray), Cyfip1 (green), Neogenin (yellow) and PSD-95 (magenta) in spines in BDNF untreated (B) and treated (C) neurons.

(D and E) Quantification of (D) Neogenin clusters and (E) Cyfip1 clusters associated with PSD-95 +/− BDNF. Unpaired Student's t test: (D) Neo only, $p < 0.0001$; $F(80, 74) = 1.817$, $p = 0.0099$; Neo+PSD-95, $p < 0.0001$; $F(74, 80) = 1.968$, $p = 0.0032$, (E) Cyfip1 only, $p < 0.0001$; $F(80, 74) = 1.817$, $p = 0.0099$; Cyfip1+PSD-95, $p < 0.0001$; $F(74, 80) = 1.968$, $p = 0.0032$. $N = 75–81$ spines, 11 neurons/condition, mean ± SEM, $^{**}p < 0.01$, $^{****}p < 0.0001$.

fraction (Figure 4H) was observed in the absence of BDNF. We conclude that efficient Neogenin trapping into WRC nanodomains on the spine membrane is mediated by its interaction with the WRC and is facilitated by BDNF. In contrast, similar analysis on dendritic shafts showed that Neogenin diffusivity was not reduced by its interaction with the WRC or exposure to BDNF as no differences were observed in the mean squared displacement (Figure 4I), the area under the curve (Figure 4J) or the immobile fraction (Figure 4K).

The aforementioned observations demonstrate that BDNF promotes diffusion trapping of Neogenin into WRC nanodomains. To determine how BDNF influences Neogenin nanocluster organization in time and space we employed nanoscale spatiotemporal indexing clustering (NASTIC).[52] Analysis of clustered trajectories revealed that Neo-mEos nanoclusters were present on the spine membrane at a mean density of 0.5 clusters/µm^2 (Figures 5A–5C). BDNF significantly increased the cluster density by 1.4-fold which was dependent on WRC binding as the NeoΔWIRS-mEos cluster density was reduced by 75% (Figure 5C). BDNF also increased the number of Neo-mEos molecules detected/cluster (cluster membership) (Figure 5D) and prolonged the apparent lifetime of Neo-mEos nanoclusters by 1.2-fold (Figure 5E). It should be noted that the BDNF-induced increase in cluster membership was not due to the merger of smaller clusters as the cluster radius was not influenced by BDNF (Figure 5F). In comparison to Neo-mEos, NeoΔWIRS-mEos cluster membership and lifetime were markedly reduced in the presence of BDNF (22.4%, and 31.8% respectively) (Figures 5D and 5E). We conclude that in response to BDNF stimulation,

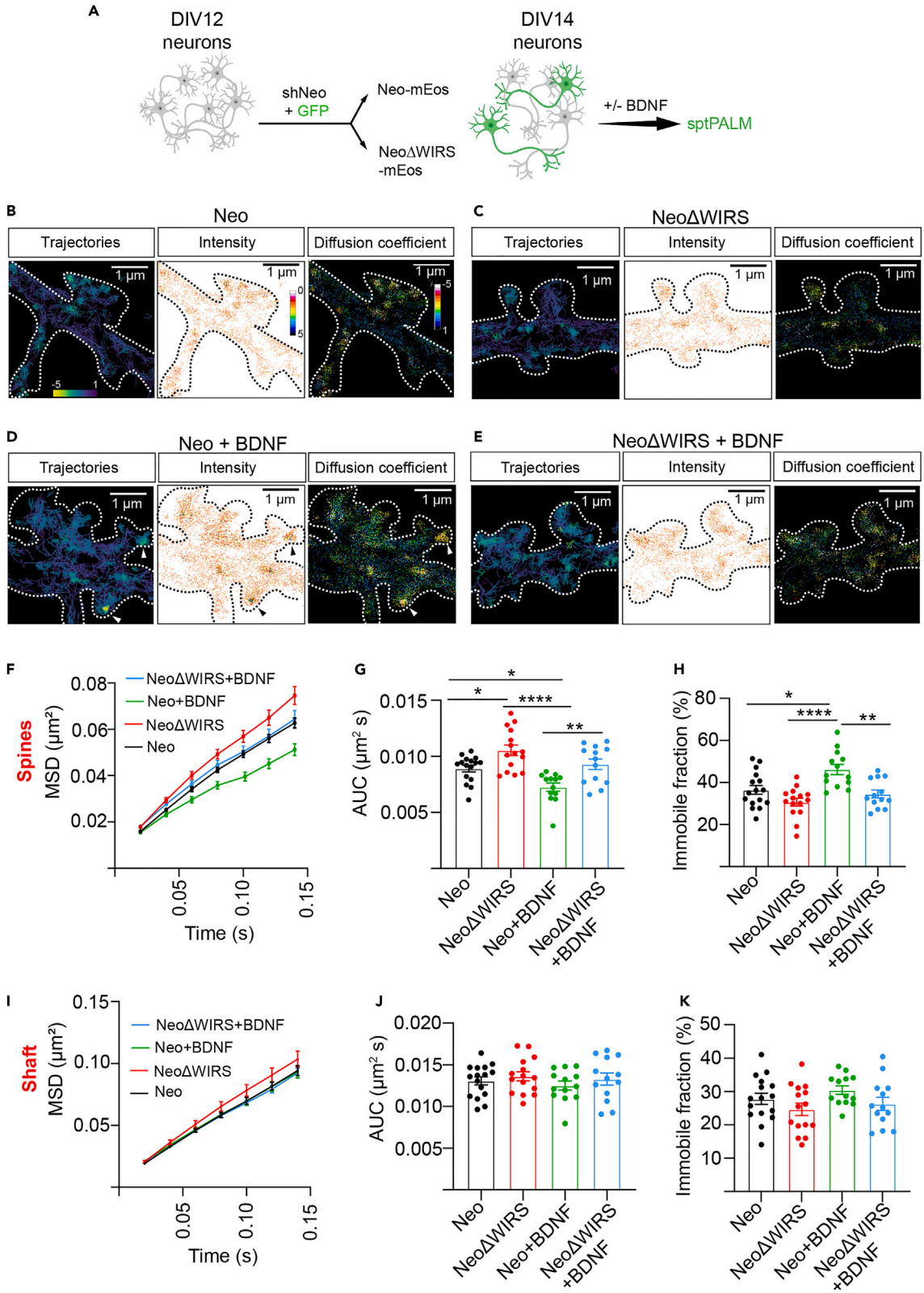
A
DIV12 neurons
shNeo + GFP
Neo-mEos
NeoΔWIRS -mEos
DIV14 neurons
+/- BDNF
sptPALM
B
Neo
C
NeoΔWIRS
D
Neo + BDNF
E
NeoΔWIRS + BDNF
Trajectories
Intensity
Diffusion coefficient
1 µm
F
Spines
MSD (µm²)
Time (s)
NeoΔWIRS+BDNF
Neo+BDNF
NeoΔWIRS
Neo
G
AUC (µm² s)
H
Immobile fraction (%)
I
Shaft
J
K
Neo
NeoΔWIRS
Neo+BDNF
NeoΔWIRS +BDNF

Figure 4. BDNF induces WRC-dependent diffusion trapping of Neogenin on spines

(A) sptPALM was performed on hippocampal spines after shRNA depletion of Neogenin and rescue with either Neo-mEos or NeoΔWIRS-mEos.

(B–E) Neo-mEos (B and D) and NeoΔWIRS-mEos (C and E) trajectory maps, localization intensity maps (blue, higher localization intensity) and diffusion coefficient maps (blue, higher mobility) in untreated (B and C) or BDNF-treated (D and E) cultures.

(F–K) Quantification of the average mean squared displacement as a function of time (F and I), mobility (area under the curve) (G and J) and immobile fraction (H and K) for spines (F–H) and shafts (I–K). Two-way ANOVA, Tukey's *post hoc* test: (G) $F1(17, 36) = 1.077$, $p = 0.4098$; $F2(3, 26) = 11.00$, $p < 0.0001$, (J) $F1(19, 34) = 1.064$, $p = 0.4247$; $F2(3, 34) = 1.345$, $p = 0.2761$, (H) $F1(17, 36) = 1.231$, $p = 0.2910$; $F2(3, 26) = 10.38$, $p < 0.0001$, (K) $F1(18, 35) = 1.711$, $p = 0.0851$; $F2(3, 35) = 3.075$, $p = 0.0402$. (F–K) $N = 13–16$ neurons, mean ± SEM, $*p < 0.05$, $**p < 0.01$, $****p < 0.0001$.

Neogenin is recruited into WRC nanodomains by diffusion trapping through its interaction with the WRC, and that the stability of the Neogenin-WRC nanoclusters is facilitated by BDNF. This further suggests that Neogenin/WRC nanodomain formation is governed by the availability of Cyfip1 which is released from the FMRP complex in response to BDNF. Neogenin binding to the WRC without BDNF treatment reduced Neo-mEos mobility (Figure 4). However, this interaction alone was not sufficient to promote the formation of Neo-mEos/WRC nanoclusters (Figures 5C–5E), suggesting that BDNF also activates other molecular pathways that influence Neogenin/WRC nanoarchitecture.

In line with our observation that Neogenin diffusivity on shafts was not affected by its interaction with the WRC or the addition of BDNF (Figures 4I–4K), the Neo-mEos nanocluster density on shafts (0.2 clusters/μm^2) was 2.8-fold lower than on spines and was not affected by BDNF or disruption to WRC binding (Figure 5G). This provides strong evidence that the formation of Neogenin/WRC nanodomains occurs specifically in spines.

Neogenin promotes nanoclustering of a WRC subpopulation on spines

The aforementioned findings demonstrate that Neogenin is recruited into WRC domains via its interaction with the WRC. To test the possibility that, conversely, Neogenin influences WRC nanoscale behavior we again turned to sptPALM where we replaced endogenous Cyfip1 with Cyfip1-mEos after shRNA Cyfip1 depletion (shCyfip1). Previous studies have demonstrated that the fusion of GFP to the Cyfip1 C-terminus does not affect WRC function.[24] shCyfip1 reduced endogenous Cyfip1 by 50% in the NE-C4 neuroepithelial cell line (Figures S4A and S4B). Similarly, shCyfip1 reduced Cyfip1 expression in hippocampal soma by 50% (Figure S4C) and in thin and mushroom spines by 35% (Figures S4D and S4E). Furthermore, after rescue with Cyfip1-mEos, Cyfip1 protein levels were restored to endogenous levels in both mushroom and thin spines (Figures S5A–S5C) where Cyfip1-mEos colocalized with endogenous WAVE1 and Neogenin (Figures S5D and S5E). As the Neogenin WIRS motif binds to the WRC only when the full pentameric complex is assembled,[19,35,46] and the vast majority of Cyfip1 is associated with the WRC after BDNF exposure,[24,25] we used Cyfip1-mEos as a proxy for the WRC in these experiments.

Initially, we compared Cyfip1 nanoscale dynamics on spines and shafts after cotransfection of shCyfip1, Cyfip1-mEos, and shNeo or shCtl (Figure S6A). Cyfip1-mEos trajectory, intensity and diffusion coefficient maps were then generated (Figures S6B–S6E). As seen for Neogenin, the molecular displacement over time (Figure S6F) and the area under the curve (mobility, Figure S6G) indicated that Cyfip1-mEos mobility was reduced by 30% in spines relative to shafts. The shift to the left for the diffusion coefficient frequency distribution curve (Figure S6H) and the 1.3-fold increase in the number of Cyfip1-mEos molecules associated with the immobile fraction (spines, 56%; shafts, 44%, Figure S6I) confirmed that Cyfip1-mEos mobility was reduced in spines. These data therefore show that, like Neo-mEos, Cyfip1-mEos is more confined at the spine membrane (Figure S6J).

We have shown that BDNF promotes the trapping of Neogenin receptors into nanodomains in a WRC-dependent manner. Therefore, conversely, Neogenin may influence WRC nanoscale mobility and organization at the spine membrane. Cyfip1-mEos super-resolved intensity, trajectory and diffusion coefficient maps were generated after cotransfection of shCyfip1, Cyfip1-mEos along with shNeo or shCtl (Figures 6A–6E). Following BDNF treatment, a significant increase in Cyfip1-mEos mobility (1.3-fold) (Figures 6F and 6G) coupled with a reduction (16%) in the immobile fraction (Figure 6H) was observed in Neogenin depleted spines, indicating that Neogenin contributed to the confinement of Cyfip1-mEos subunits within nanodomains. A similar trend was noted without BDNF treatment. In contrast to the spine, BDNF significantly increased the mobility (Figures 6I and 6J) and decreased the immobile fraction of Cyfip1-mEos in shafts (Figure 6K). However, this effect was not dependent on Neogenin-WRC interactions, suggesting that BDNF acts through a different pathway in shafts.

To gain further insight into the spatiotemporal parameters underlying Cyfip1-mEos nano-organization in the spine, we again used NASTIC analysis. Although BDNF failed to decrease Cyfip1-mEos mobility below control levels (Figures 6F–6H), the addition of BDNF markedly increased Cyfip1 nanocluster density (4.3 clusters/μm^2, 1.3-fold increase; Figures 7A–7C). This effect was reversed by Neogenin depletion (2.1 clusters/μm^2, 52% decrease; Figures 7B and 7C). However, as Cyfip1-mEos cluster membership was not influenced by BDNF or the depletion of Neogenin (Figures 7D–7F), it is likely that other WRC-binding partners are also necessary for WRC nanodomain formation and stability in the spine. As seen for Neo-mEos, neither loss of Neogenin nor the addition of BDNF significantly influenced clustering on shafts (Figure 7G). Together, these observations demonstrate that Neogenin is required for the formation of WRC nanoclusters specifically in spines.

Neogenin-WRC interactions are required for BDNF-induced actin polymerization and calcium signaling

BDNF facilitates actin remodeling through the redistribution of Cyfip1 from FMRP to the WRC at the spine membrane.[16,24,25] We therefore assessed whether BDNF-mediated actin polymerization was dependent on Neogenin-WRC interactions using FRAP (fluorescence recovery

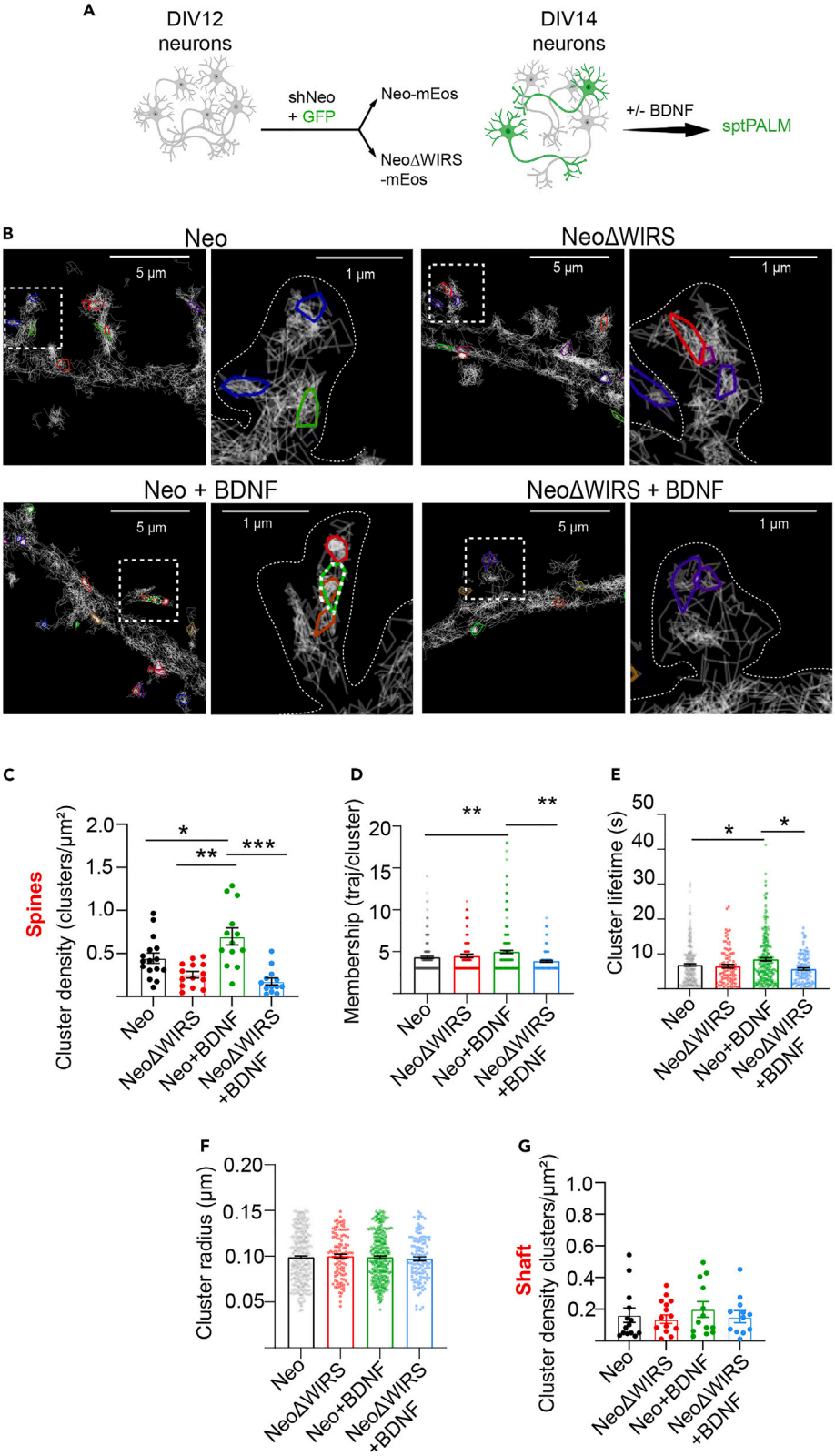
A
DIV12 neurons
shNeo + GFP
Neo-mEos
NeoΔWIRS -mEos
DIV14 neurons
+/- BDNF
sptPALM
B
Neo
NeoΔWIRS
Neo + BDNF
NeoΔWIRS + BDNF
5 µm
1 µm
C
Spines
Cluster density (clusters/µm²)
D
Membership (traj/cluster)
E
Cluster lifetime (s)
F
Cluster radius (µm)
G
Shaft
Cluster density clusters/µm²)
Neo
NeoΔWIRS
Neo+BDNF
NeoΔWIRS +BDNF

Figure 5. BDNF induces WRC-dependent Neogenin nanoclustering on spines

(A) NASTIC analysis of hippocampal spines after shRNA depletion of Neogenin and rescue with either Neo-mEos or NeoΔWIRS-mEos.

(B) Representative images of the distribution of Neo and NeoΔWIRS trajectories and nanoclusters (outlined in color) in BDNF untreated and treated neurons.

(C–G) BDNF induces nanoclustering in spines (C–F) but not shafts (G). Quantification of cluster density (C and G), cluster membership (D), cluster lifetime (E), and cluster radius (F). Two-way ANOVA, Tukey's *post hoc* test: (C) $F1(18, 34) = 1.546$, $p = 0.1336$; $F2(3, 34) = 8.752$, $p = 0.0002$, (G) $F1(17, 27) = 0.9043$, $p = 0.5765$; $F2(3, 27) = 0.2020$, $p = 0.8941$, (D) $F1(367, 379) = 1.189$, $p = 0.0478$; $F2(3, 379) = 5.564$, $p = 0.0010$, (E) $F1(359, 384) = 1.130$, $p = 0.1198$; $F2(3, 384) = 4.498$, $p = 0.0041$, (F) $F1(371, 388) = 1.169$, $p = 0.0638$; $F2(3, 388) = 1.065$, $p = 0.3640$. (C and G) $N = 13–14$ neurons. (D–F) Neo ($N = 6,947$ trajectories, 286 clusters), NeoΔWIRS ($N = 3,383$ trajectories, 99 clusters), Neo + BDNF ($N = 6,840$ trajectories, 255 clusters) and NeoΔWIRS + BDNF ($N = 4,709$ trajectories, 114 clusters). (C–G) Mean ± SEM, $*p < 0.05$, $**p < 0.01$, $***p < 0.001$.

after photobleaching). shRNAs and the Neo constructs (without mEos) were transfected into DIV12 hippocampal neurons along with LifeAct-RFP (Figure 8A). BDNF was applied at DIV14, spines were then photobleached and LifeAct-RFP fluorescence recovery monitored for 150 s.[53] As expected, the addition of BDNF increased the pool of stable actin (stable fraction) by 1.4-fold above control levels (Figures 8B and 8C), confirming that BDNF enhances actin polymerization. BDNF-induced polymerization was significantly reduced (44%) in shNeo-expressing spines, an effect that was rescued by wild-type Neo but not NeoΔWIRS (Figures 8D–8F). Neogenin depletion had no effect in the absence of BDNF (Figures 8G and 8H). Therefore, BDNF-facilitated actin remodeling in spines requires the Neogenin-WRC interaction.

The aforementioned sptPALM and FRAP studies provide strong evidence that BDNF promotes the nanoclustering of Neogenin and the WRC, leading to actin polymerization. This suggests that BDNF enhances Neogenin-WRC interactions. To test this, we asked whether BDNF increased the frequency of endogenous Neogenin-WRC interactions using the proximity ligation assay. Upon the addition of BDNF, a significant 1.3-fold increase in the number of endogenous Neogenin/Cyfip1 PLA puncta was observed in hippocampal spines (Figures S7A–S7C), demonstrating that Neogenin-WRC interactions are indeed augmented by BDNF.

The actin cytoskeleton plays a central role in anchoring many postsynaptic receptors, including glutamate receptors, to the PSD scaffolding. Disruption of these interactions directly impacts postsynaptic calcium signaling.[54,55] It is therefore possible that perturbation of Neogenin-WRC-mediated actin remodeling affects other BDNF signaling pathways such as the induction of calcium fluxes. To test this possibility, shRNAs and the Neo constructs were transfected into DIV12 hippocampal neurons along with the fRGECO1 calcium sensor,[56] and BDNF applied at DIV14 (Figure 8I). The change in calcium fluorescence was quantified over the first 5 s post-application by expressing the mean peak fluorescence intensity induced by BDNF relative to basal levels (ΔF/F0). BDNF elicited a strong calcium rise in control spines which was reduced 3.1-fold by Neogenin depletion (Figures 8J and 8K). The BDNF-evoked transients were fully restored by Neo-mEos expression whereas NeoΔWIRS-mEos failed to reinstate the calcium response (Figures 8J and 8K). Therefore, these data demonstrate that Neogenin-WRC interactions promote BDNF-induced calcium elevation and that blocking these interactions impedes postsynaptic calcium signaling.

DISCUSSION

Tight spatiotemporal control of actin regulators at the nanoscale level is critical for activity-dependent actin remodeling and therefore structural plasticity.[8,55] The WRC, a pivotal actin regulator, is confined to stable nanodomains at the postsynaptic membrane where it catalyzes Arp2/3-mediated branched actin polymerization. Our recent demonstration that Neogenin is a key regulator of spine enlargement through its ability to activate WRC-mediated actin polymerization[43] suggests that the nanoscale organization of Neogenin is likely to be an important mechanism governing actin remodeling and may also be a determinant of WRC nanoarchitecture. However, the nanoscale behavior of Neogenin has not been explored. Here, we reveal that Neogenin, is highly organized on the spine membrane at the nanoscale level. We demonstrate that Neogenin binding to the WRC promotes Neogenin/WRC nanodomain assembly. Importantly, we show that nanodomain formation is regulated by BDNF, indicating that nanoclustering occurs in response to synaptic stimulation. Finally, we show that the Neogenin-WRC interaction facilitates BDNF-mediated actin remodeling and induction of calcium signaling, suggesting that the assembly of Neogenin/WRC nanodomains is a prerequisite for BDNF-mediated structural and synaptic plasticity.

Nanoscale alignment of presynaptic glutamate release sites with postsynaptic ion channels and associated PSD scaffold proteins (trans-synaptic nanocolumns) underlies efficient synaptic transmission.[27,28,30,57] We demonstrate using super-resolution microscopy that Neogenin is confined within two distinct nanocluster populations where 23% of clusters are encircled by ring-like WRC nanodomains. The clustering of Neogenin and the WRC into nanodomains was confirmed by single-particle tracking which demonstrated that Neogenin nanocluster density and stability were dependent on the interaction between Neogenin's cytoplasmic WIRS motif and the WRC. Similarly, the density of WRC nanodomains was found to be dependent on the presence of Neogenin. The functional relevance of the Neogenin-WRC interactions was substantiated by the demonstration that mutations in the WIRS motif prevented actin polymerization in the spine. Simple ground rules are now emerging for the nanoscale behavior of PSD-resident proteins. On average, up to four PSD-95 or glutamate receptor nanomodules are observed on the spine membrane, where an increase in nanomodule number but not size is correlated with increased synaptic strength.[27,28,45] We found that Neogenin exhibited similar nanoscale behaviors, suggesting that Neogenin-WRC nanoclusters may participate in trans-synaptic nanocolumns. The number of Neogenin and WRC nanodomains was found to scale with increasing spine size and BDNF stimulation increased the density but not the diameter of nanodomains. We therefore conclude that Neogenin is tethered within WRC nanodomains where it is perfectly positioned to regulate WRC-mediated actin polymerization at the PSD.

What then are the molecular events driving the clustering of Neogenin and the WRC into a single nanodomain? Diffusion trapping, the capture of diffusing molecules by binding partners, is an important mechanism determining synaptic nanoarchitecture.[29,58] BDNF was found to decrease the mobility of Neogenin on the postsynaptic membrane, promote its incorporation into nanoclusters, and increase cluster

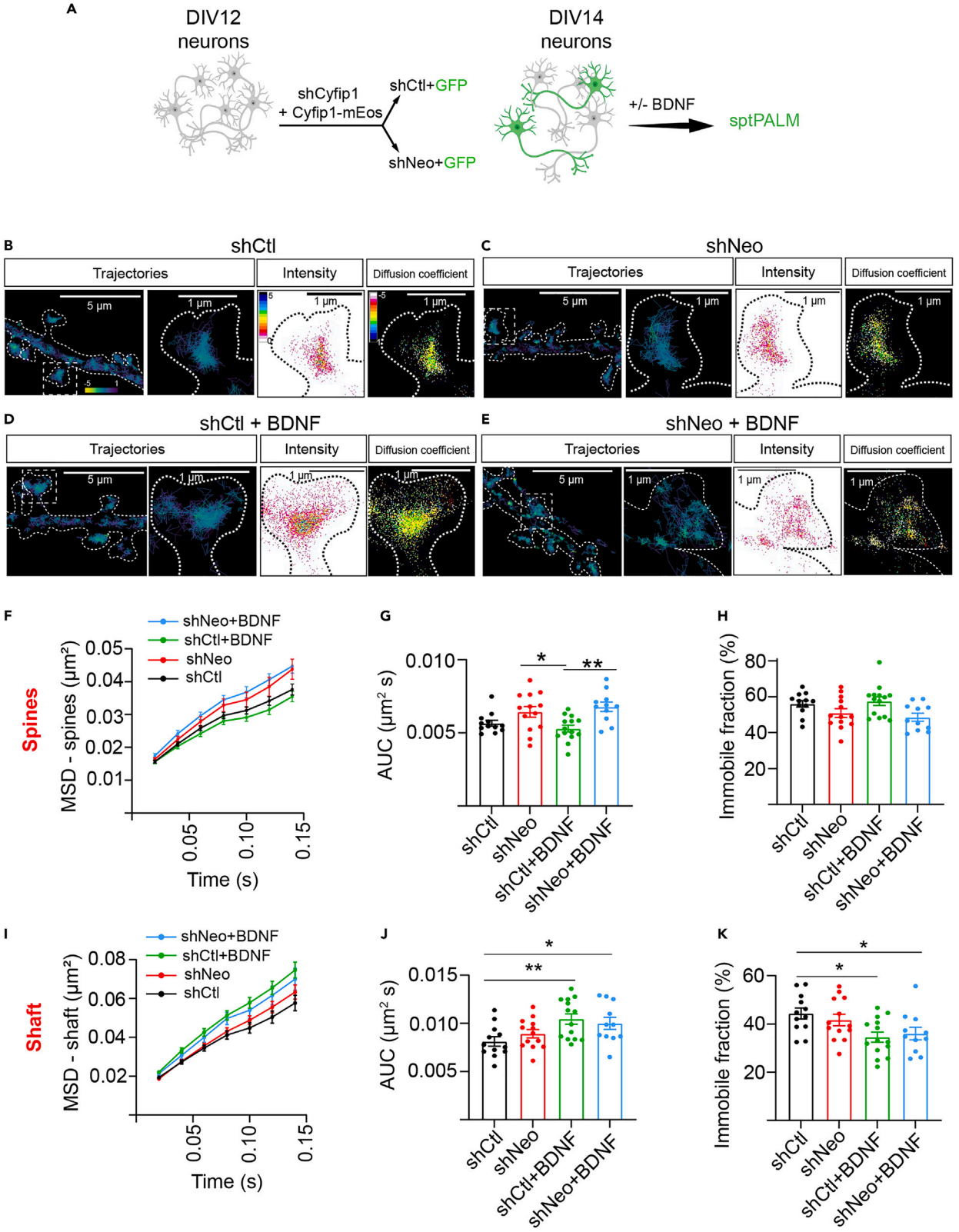
A
DIV12 neurons
shCyfip1 + Cyfip1-mEos
shCtl+GFP
shNeo+GFP
DIV14 neurons
+/- BDNF
sptPALM
B
shCtl
C
shNeo
Trajectories
Intensity
Diffusion coefficient
5 µm
1 µm
D
shCtl + BDNF
E
shNeo + BDNF
F
Spines
MSD - spines (µm²)
Time (s)
shNeo+BDNF
shCtl+BDNF
shNeo
shCtl
G
AUC (µm² s)
H
Immobile fraction (%)
I
Shaft
MSD - shaft (µm²)
J
K

Figure 6. WRC diffusion trapping is dependent on Neogenin in spines

(A) sptPALM was performed on hippocampal spines after cotransfection with Cyfip1 shRNA, Cyfip1-mEos, and Neo (shNeo) or control shRNA (shCtl).

(B–E) (B and D) shCtl and (C and E) shNeo trajectory maps, localization intensity maps (blue, higher localization intensity) and diffusion coefficient maps (blue, higher mobility) in untreated (B and C) or BDNF-treated (D and E) neurons.

(F–K) Quantification of the average mean squared displacement as a function of time (F and I), mobility (area under the curve) (G and J), and immobile fraction (H and K) for spines (F–H) and shafts (I–K). Two-way ANOVA, Tukey's *post hoc* test: (G) $F1(18, 28) = 0.9875$, $p = 0.4992$; $F2(3, 28) = 6.017$, $p = 0.0027$, (J) $F1(15, 31) = 1.980$, $p = 0.0528$; $F2(3, 31) = 4.538$, $p = 0.0095$, (H) $F1(18, 28) = 0.6421$, $p = 0.8351$; $F2(3, 28) = 2.882$, $p = 0.0535$, (K) $F1(15, 31) = 1.989$, $p = 0.0518$; $F2(3, 31) = 3.765$, $p = 0.0205$. (F–K) $N = 11–14$ neurons, mean ± SEM, $^{*}p < 0.05$, $^{**}p < 0.01$. Also see Figures S4–S6.

density and longevity — nanoscale behaviors that were not observed for the WIRS mutant. These observations provide compelling evidence that in the presence of BDNF, Neogenin undergoes diffusion trapping via its WIRS motif, leading to the formation of stable co-clustered nanodomains. In contrast, no increase in Neogenin/WRC nanodomain density was observed in the absence of BDNF. BDNF ensures WRC availability at the PSD by triggering the redistribution of Cyfip1 from the FMRP translational repressor complex.[12,16,18,24,25,59] This argues that Neogenin diffusion trapping is dependent on the WRC concentration at the PSD and is therefore sensitive to BDNF release from the pre- and/or postsynaptic compartment. Neither BDNF nor mutations in the WIRS motif influenced Neogenin behavior on the shaft, indicating that Neogenin/WRC nanoarchitecture is tightly regulated by BDNF specifically in the spine.

Given that a substantial proportion of WRC nanodomains (43%) is associated with Neogenin, we also investigated whether Neogenin influences WRC nanoscale organization. Consistent with this hypothesis, loss of Neogenin reduced Cyfip1 nanocluster density at the postsynaptic membrane in the presence of BDNF. This supports the conclusion that Neogenin regulates WRC nanoarchitecture at the PSD by anchoring a subpopulation of WRC pentamers within nanoclusters. A previous study has shown that the WRC is confined to nanodomains overlapping the PSD in close proximity to its upstream activator Rac1 and its downstream effector Arp2/3.[31] It has also been shown in fibroblast lamellipodia that WRC diffusion trapping into nanoscale rings is required for optimal Arp2/3 activation and that the cluster dwell time correlates with the extent of Arp2/3-mediated actin nucleation.[33] However, the mechanism underlying WRC nanoscale dynamics has not been identified. We propose that Neogenin fulfills this role in the spine. Moreover, Neogenin controls WRC activity in other neural and non-neural cell types,[35,46] suggesting that Neogenin/WRC nanoscale organization is likely to be a general mechanism regulating actin remodeling in many tissues.

We note that Neogenin-induced WRC clustering was less predominant when compared to WRC-mediated diffusion trapping of Neogenin, indicating that other PSD proteins influence WRC nanoarchitecture and dynamics. This was substantiated by the finding that 57% of Cyfip1 nanodomains were not associated with Neogenin. Many postsynaptic proteins including WIRS-containing receptors and PSD scaffold proteins are known to form complexes with the WRC.[19,60] One potential candidate is the I-BAR protein IRSp53 which links the WRC to the plasma membrane and is confined to persistent nanodomains overlapping the WRC at the PSD.[31] In addition, WIRS-containing proteins such as the Neuroligin adhesion receptors and the Shank scaffold proteins also functionally interact with the WRC at the PSD.[19,60]

Our finding that Neogenin-WRC binding is required for BDNF induction of calcium fluxes provides evidence that Neogenin/WRC nanoarchitecture also impacts BDNF-mediated synaptic plasticity and identifies Neogenin as a downstream effector of BDNF-induced calcium signaling. As such, these observations offer mechanistic insight into Neogenin's role in LTP. Neogenin is required for LTP induction and maintenance, and its loss leads to deficits in memory retrieval and depressive-like behaviors.[41,61] Neogenin is also essential for the induction of LTP at the entorhinal to granule cell synapse within the dentate gyrus where it forms a trans-synaptic adhesion complex with presynaptic neurexin-1 via its secreted ligand cerebellin-4.[42] We therefore propose that Neogenin/Neurexin nanocolumns couple synaptic adhesion with WRC-mediated actin remodeling at the PSD. Neurexins also form trans-synaptic nanocolumns with their postsynaptic binding partners, the neuroligins, to promote active zone assembly and AMPA receptor alignment with presynaptic glutamate release sites.[57,62,63] Intriguingly, neuroligin also directly binds the WRC via its WIRS motif,[19,64] further suggesting that Neogenin and neuroligins may coexist in the same WRC nanodomains. We therefore propose a testable model in which Neogenin/Neurexin nanocolumns synchronize pre- and postsynaptic functions, thereby coordinating the induction of structural plasticity and synaptic activation. Furthermore, many other important synaptic proteins (the NR2B subunit of the NMDA receptor, mGluR5 and 6, potassium voltage-gated channels, protocadherins, the DCC netrin receptor) contain the WIRS motif.[19] Therefore, the insights gained in our study identify a unique nanoscale mechanism through which these proteins may promote structural and functional plasticity.

Limitations of the study

BDNF reinforces synaptic strength by ensuring that actin polymerization is promoted in the spine-head by increasing Cyfip1 availability and thus WRC formation at the PSD.[24,25] We show that Neogenin-mediated WRC co-clustering into nanodomains is a downstream effect of BDNF release. Our data also indicate that the nanodynamics of the WRC is modulated by other as yet unidentified interactors where 57% of WRC clusters are not associated with Neogenin. This raises intriguing questions not addressed in our study. What is the identity of these unknown modulators and through which postsynaptic pathways are they activated? The NR2B subunit of the NMDA receptor and the mGluR5 metabotropic receptor subunit possess WIRS motifs. It is therefore plausible that synaptic stimulation may directly influence WRC nanodynamics via activation of these key ion channels. This further suggests that the relative activity of these channels may fine-tune WRC activity and actin remodeling to ensure structural plasticity is exquisitely responsive to the postsynaptic milieu. A second intriguing finding is that 77% of Neogenin nanoclusters form independently of the WRC, a phenomenon specifically confined to the postsynaptic membrane. Several questions then emerge: what is the function of these nanoclusters, which Neogenin interactors control their nanoarchitecture and what is their

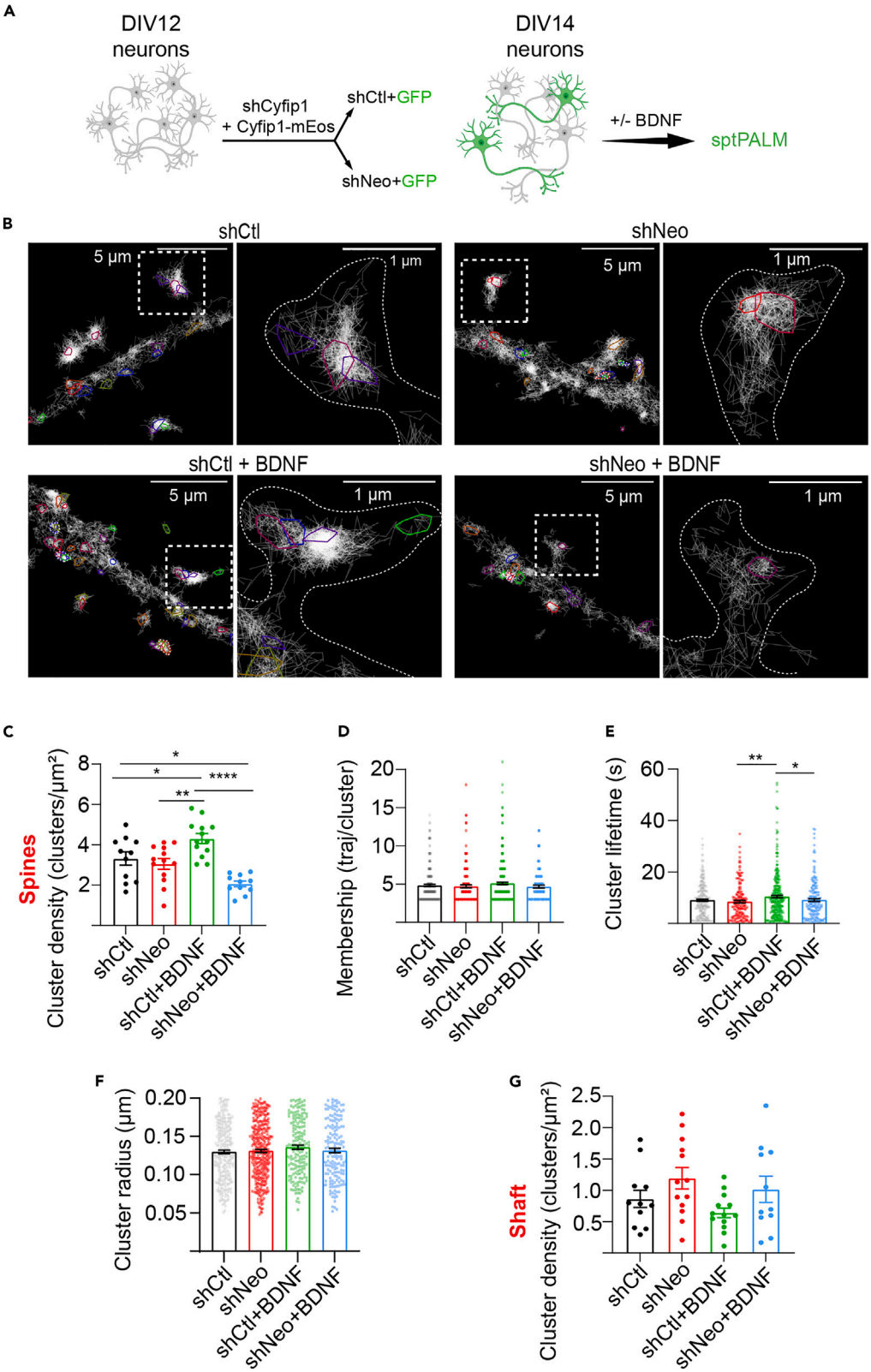
A
DIV12 neurons
shCyfip1 + Cyfip1-mEos
shCtl+GFP
shNeo+GFP
DIV14 neurons
+/- BDNF
sptPALM
B
shCtl
shNeo
shCtl + BDNF
shNeo + BDNF
5 µm
1 µm
C
Spines
Cluster density (clusters/µm²)
D
Membership (traj/cluster)
E
Cluster lifetime (s)
F
Cluster radius (µm)
G
Shaft
Cluster density (clusters/µm²)
shCtl
shNeo
shCtl+BDNF
shNeo+BDNF

Figure 7. Neogenin promotes nanoclustering of the WRC in the presence of BDNF

(A) NASTIC analysis of hippocampal spines after cotransfection with Cyfip1 shRNA, Cyfip1-mEos, and Neo (shNeo) or control shRNA (shCtl).

(B) Representative images of the distribution of Cyfip1-mEos trajectories and nanoclusters (outlined in color) +/− BDNF.

(C–G) BDNF increases Cyfip1-mEos nanocluster density in spines (C) but not shafts (G). Quantification of cluster density (C and G), cluster membership (D), cluster lifetime (E), and cluster radius (F). Two-way ANOVA, Tukey's *post hoc* test: (C) $F1(13, 31) = 1.332$, $p = 0.2479$; $F2(3, 31) = 13.19$, $p < 0.0001$, (G) $F1(15, 31) = 0.4047$, $p = 0.9668$; $F2(3, 31) = 1.357$, $p = 0.2740$, (D) $F1(279, 596) = 0.8803$, $p = 0.8886$; $F2(3, 596) = 2.281$, $p = 0.0782$, (E) $F1(279, 603) = 0.9491$, $p = 0.6898$; $F2(3, 603) = 4.410$, $p = 0.0044$, (F) $F1(279, 603) = 0.9545$, $p = 0.6704$; $F2(3, 603) = 3.880$, $p = 0.0091$. (C and G) $N = 11–13$ neurons. (D–F) shCtl ($N = 4,325$ trajectories, 256 clusters), shNeo ($N = 2,667$ trajectories, 172 clusters), shCtl + BDNF ($N = 6,425$ trajectories, 334 clusters) and shNeo + BDNF ($N = 2,390$ trajectories, 178 clusters). Mean ± SEM, $*p < 0.05$, $**p < 0.01$, $****p < 0.0001$.

relationship to WRC function and nanodynamics? Answers to the aforementioned questions are required if we are to further advance our understanding of the molecular mechanisms governing structural and synaptic plasticity.

STAR★METHODS

Detailed methods are provided in the online version of this paper and include the following:

- KEY RESOURCES TABLE
- RESOURCES AVAILABILITY
  - Lead contact
  - Materials availability
  - Data and code availability
- EXPERIMENTAL MODEL AND STUDY PARTICIPANTS
- METHOD DETAILS
  - Neuronal transfection
  - Constructs and shRNAs
  - Analysis of shRNA efficiency
  - Immunocytochemistry
  - Spine analysis
  - BDNF stimulation
  - Proximity ligation assay
  - Fluorescence recovery after photo bleaching
  - Calcium imaging
  - Stochastic optical reconstruction microscopy (STORM)
  - Single-particle tracking using photoactivation localization microscopy (sptPALM)
- QUANTIFICATION AND STATISTICAL ANALYSIS

SUPPLEMENTAL INFORMATION

Supplemental information can be found online at https://doi.org/10.1016/j.isci.2024.110621.

ACKNOWLEDGMENTS

This work was supported by the National Health and Medical Research Council of Australia (grants 1181459, 2001024, and 2010901). F.A.M. was supported by a National Health and Medical Research Council of Australia Fellowship (grant 1155794). NASTIC development by F.A.M. and T.P.W. was supported by the National Institutes of Health, United States (R21 Grant RM2022000288). We are grateful to Frank and Patsy Youngleson for their generous support through a private donation. Imaging work was performed in the Queensland Brain Institute's Advanced Microscopy Facility and generously supported by an Australian Research Council LIEF grant (LE130100078) and The University of Queensland Strategic Initiatives Fund (DVCR22052A). We thank Dr Rumelo Amor, Dr Arnaud Gaudin, and Dr Andrew Thompson for their expert microscopy advice.

AUTHOR CONTRIBUTIONS

B.S. performed all experiments. T.P.W., F.A.M., and N.D. provided advice on experimental design and data interpretation. E.O.B. and K.S. provided technical assistance. B.S., H.M.C., and C.F. contributed to experimental design and data analysis. H.M.C. and B.S. wrote the manuscript with contributions from all authors. All authors approved the submitted manuscript.

DECLARATION OF INTERESTS

The authors declare no conflicts of interest.

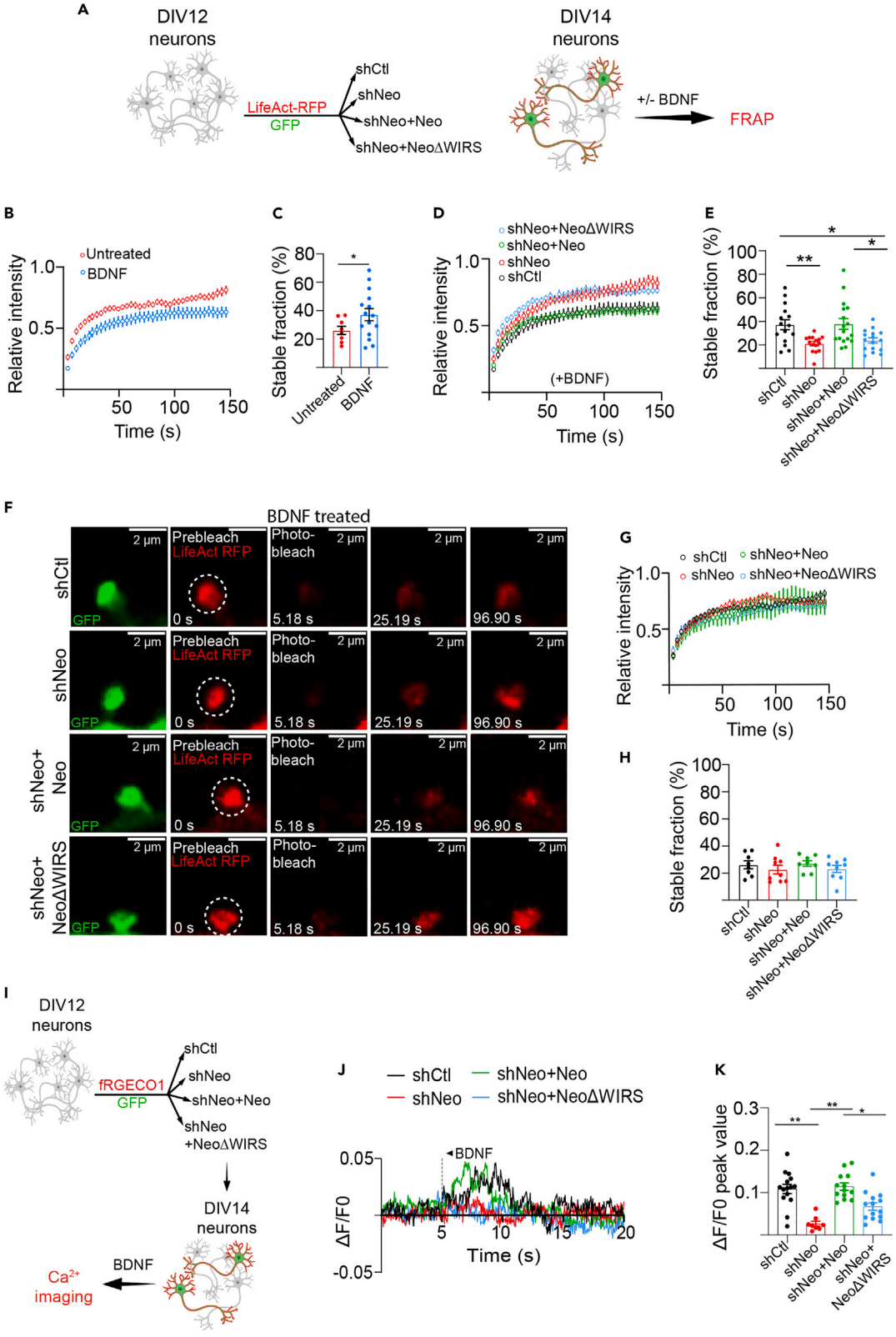
A
DIV12 neurons
LifeAct-RFP
GFP
shCtl
shNeo
shNeo+Neo
shNeo+NeoΔWIRS
DIV14 neurons
+/- BDNF
FRAP
B
Untreated
BDNF
Relative intensity
Time (s)
C
Stable fraction (%)
Untreated
BDNF
D
shNeo+NeoΔWIRS
shNeo+Neo
shNeo
shCtl
(+BDNF)
Relative intensity
Time (s)
E
Stable fraction (%)
shCtl
shNeo
shNeo+Neo
shNeo+NeoΔWIRS
F
BDNF treated
shCtl
shNeo
shNeo+ Neo
shNeo+ NeoΔWIRS
2 μm
Prebleach
LifeAct RFP
Photo-bleach
GFP
0 s
5.18 s
25.19 s
96.90 s
G
shCtl
shNeo
shNeo+Neo
shNeo+NeoΔWIRS
Relative intensity
Time (s)
H
Stable fraction (%)
shCtl
shNeo
shNeo+Neo
shNeo+NeoΔWIRS
I
DIV12 neurons
fRGECO1
GFP
shCtl
shNeo
shNeo+Neo
shNeo +NeoΔWIRS
DIV14 neurons
BDNF
Ca2+ imaging
J
shCtl
shNeo
shNeo+Neo
shNeo+NeoΔWIRS
BDNF
ΔF/F0
Time (s)
K
ΔF/F0 peak value
shCtl
shNeo
shNeo+Neo
shNeo+ NeoΔWIRS

Figure 8. Neogenin-WRC interactions are required for BDNF-induced actin polymerization and calcium signaling

(A) FRAP analysis of LifeAct-RFP-transfected hippocampal spines after shRNA depletion of Neogenin and rescue with either Neo-mEos or NeoΔWIRS-mEos.

(B) Relative intensity curve showing F-actin recovery in shCtl spines before and after BDNF treatment.

(C) Quantification of the stable F-actin fraction (unpaired Welch's t test, $p = 0.0448$; $F(14, 7) = 3.996$, $p = 0.0726$, $N = 8–15$ neurons).

(D) Relative intensity curve after BDNF addition showing F-actin recovery in the presence of Neo-mEos but not NeoΔWIRS-mEos.

(E) Quantification of the stable F-actin fraction.

(F) Representative FRAP images for (D).

(G) Relative intensity curve showing F-actin recovery in the presence of Neo-mEos or NeoΔWIRS-mEos without BDNF.

(H) Quantification of the stable F-actin fraction.

(I) Schematic outlines the experimental workflow in J and K.

(J and K) Relative fluorescence intensities (ΔF/F0) of calcium rises in response to BDNF. One-way ANOVA, Tukey's *post hoc* test: (E) $F = 6.385$, $p = 0.0008$; $F(3, 59) = 3.802$, $p = 0.0147$, $N = 15–17$ neurons, (H) $F = 0.6156$, $p = 0.6103$; $F = 6.385$, $F(3, 30) = 0.5987$, $p = 0.6208$, $N = 8–9$ neurons), (K) $F = 15.39$, $p < 0.0001$; $F(3, 46) = 1.176$, $p = 0.3290$, $N = 10–15$ neurons. Mean ± SEM, $^*p < 0.05$, $^{**}p < 0.01$. Also see Figure S7.

Received: February 22, 2024
Revised: June 1, 2024
Accepted: July 26, 2024
Published: July 30, 2024

REFERENCES

1. Tanaka, J.-I., Horiike, Y., Matsuzaki, M., Miyazaki, T., Ellis-Davies, G.C.R., and Kasai, H. (2008). Protein synthesis and neurotrophin-dependent structural plasticity of single dendritic spines. Science *319*, 1683–1687.
2. Bourne, J.N., and Harris, K.M. (2011). Coordination of size and number of excitatory and inhibitory synapses results in a balanced structural plasticity along mature hippocampal CA1 dendrites during LTP. Hippocampus *21*, 354–373.
3. Harvey, C.D., and Svoboda, K. (2007). Locally dynamic synaptic learning rules in pyramidal neuron dendrites. Nature *450*, 1195–1200.
4. Matsuzaki, M., Honkura, N., Ellis-Davies, G.C.R., and Kasai, H. (2004). Structural basis of long-term potentiation in single dendritic spines. Nature *429*, 761–766.
5. Watson, D.J., Ostroff, L., Cao, G., Parker, P.H., Smith, H., and Harris, K.M. (2016). LTP enhances synaptogenesis in the developing hippocampus. Hippocampus *26*, 560–576.
6. Korobova, F., and Svitkina, T. (2010). Molecular architecture of synaptic actin cytoskeleton in hippocampal neurons reveals a mechanism of dendritic spine morphogenesis. Mol. Biol. Cell *21*, 165–176.
7. Hotulainen, P., Llano, O., Smirnov, S., Tanhuanpää, K., Faix, J., Rivera, C., and Lappalainen, P. (2009). Defining mechanisms of actin polymerization and depolymerization during dendritic spine morphogenesis. J. Cell Biol. *185*, 323–339.
8. Bosch, M., Castro, J., Saneyoshi, T., Matsuno, H., Sur, M., and Hayashi, Y. (2014). Structural and molecular remodeling of dendritic spine substructures during long-term potentiation. Neuron *82*, 444–459.
9. Okamoto, K.I., Nagai, T., Miyawaki, A., and Hayashi, Y. (2004). Rapid and persistent modulation of actin dynamics regulates postsynaptic reorganization underlying bidirectional plasticity. Nat. Neurosci. *7*, 1104–1112.
10. Honkura, N., Matsuzaki, M., Noguchi, J., Ellis-Davies, G.C.R., and Kasai, H. (2008). The subspine organization of actin fibers regulates the structure and plasticity of dendritic spines. Neuron *57*, 719–729.
11. Okamoto, K., Bosch, M., and Hayashi, Y. (2009). The roles of CaMKII and F-actin in the structural plasticity of dendritic spines: a potential molecular identity of a synaptic tag? Physiology *24*, 357–366.
12. Harward, S.C., Hedrick, N.G., Hall, C.E., Parra-Bueno, P., Milner, T.A., Pan, E., Laviv, T., Hempstead, B.L., Yasuda, R., and McNamara, J.O. (2016). Autocrine BDNF–TrkB signalling within a single dendritic spine. Nature *538*, 99–103.
13. Horvath, P.M., Chanaday, N.L., Alten, B., Kavalali, E.T., and Monteggia, L.M. (2021). A subthreshold synaptic mechanism regulating BDNF expression and resting synaptic strength. Cell Rep. *36*, 109467.
14. Lin, P.-Y., Kavalali, E.T., and Monteggia, L.M. (2018). Genetic dissection of presynaptic and postsynaptic BDNF-TrkB signaling in synaptic efficacy of CA3-CA1 synapses. Cell Rep. *24*, 1550–1561.
15. Hartmann, M., Heumann, R., and Lessmann, V. (2001). Synaptic secretion of BDNF after high-frequency stimulation of glutamatergic synapses. EMBO J. *20*, 5887–5897.
16. Panja, D., Kenney, J.W., D'Andrea, L., Zalfa, F., Vedeler, A., Wibrand, K., Fukunaga, R., Bagni, C., Proud, C.G., and Bramham, C.R. (2014). Two-stage translational control of dentate gyrus LTP consolidation is mediated by sustained BDNF-TrkB signaling to MNK. Cell Rep. *9*, 1430–1445.
17. Wang, C.S., Kavalali, E.T., and Monteggia, L.M. (2022). BDNF signaling in context: From synaptic regulation to psychiatric disorders. Cell *185*, 62–76.
18. Rex, C.S., Lin, C.-Y., Kramár, E.A., Chen, L.Y., Gall, C.M., and Lynch, G. (2007). Brain-derived neurotrophic factor promotes long-term potentiation-related cytoskeletal changes in adult hippocampus. J. Neurosci. *27*, 3017–3029.
19. Chen, B., Brinkmann, K., Chen, Z., Pak, C.W., Liao, Y., Shi, S., Henry, L., Grishin, N.V., Bogdan, S., and Rosen, M.K. (2014). The WAVE Regulatory Complex links diverse receptors to the actin cytoskeleton. Cell *156*, 195–207.
20. Kim, Y., Sung, J.Y., Ceglia, I., Lee, K.-W., Ahn, J.-H., Halford, J.M., Kim, A.M., Kwak, S.P., Park, J.B., Ho Ryu, S., et al. (2006). Phosphorylation of WAVE1 regulates actin polymerization and dendritic spine morphology. Nature *442*, 814–817.
21. Kim, I.H., Rácz, B., Wang, H., Burianek, L., Weinberg, R., Yasuda, R., Wetsel, W.C., and Soderling, S.H. (2013). Disruption of Arp2/3 results in asymmetric structural plasticity of dendritic spines and progressive synaptic and behavioral abnormalities. J. Neurosci. *33*, 6081–6092.
22. Soderling, S.H., Guire, E.S., Kaech, S., White, J., Zhang, F., Schutz, K., Langeberg, L.K., Banker, G., Raber, J., and Scott, J.D. (2007). A WAVE-1 and WRP signaling complex regulates spine density, synaptic plasticity, and memory. J. Neurosci. *27*, 355–365.
23. Spence, E.F., Kanak, D.J., Carlson, B.R., and Soderling, S.H. (2016). The Arp2/3 complex is essential for distinct stages of spine synapse maturation, including synapse unsilencing. J. Neurosci. *36*, 9696–9709.
24. De Rubeis, S., Pasciuto, E., Li, K.W., Fernández, E., Di Marino, D., Buzzi, A., Ostroff, L.E., Klann, E., Zwartkruis, F.J.T., Komiyama, N.H., et al. (2013). CYFIP1 coordinates mRNA translation and cytoskeleton remodeling to ensure proper dendritic spine formation. Neuron *79*, 1169–1182.
25. Napoli, I., Mercaldo, V., Boyl, P.P., Eleuteri, B., Zalfa, F., De Rubeis, S., Di Marino, D., Mohr, E., Massimi, M., Falconi, M., et al. (2008). The fragile X syndrome protein represses activity-dependent translation through CYFIP1, a new 4E-BP. Cell *134*, 1042–1054.
26. Genheden, M., Kenney, J.W., Johnston, H.E., Manousopoulou, A., Garbis, S.D., and Proud, C.G. (2015). BDNF stimulation of protein synthesis in cortical neurons requires the MAP kinase-interacting kinase MNK1. J. Neurosci. *35*, 972–984.
27. Hruska, M., Henderson, N., Le Marchand, S.J., Jafri, H., and Dalva, M.B. (2018). Synaptic nanomodules underlie the organization and plasticity of spine synapses. Nat. Neurosci. *21*, 671–682.
28. Hruska, M., Cain, R.E., and Dalva, M.B. (2022). Nanoscale rules governing the organization of glutamate receptors in spine synapses are subunit specific. Nat Comm *13*, 920.
29. Biederer, T., Kaeser, P.S., and Blanpied, T.A. (2017). Transcellular nanoalignment of synaptic function. Neuron *96*, 680–696.

30. Tang, A.H., Chen, H., Li, T.P., Metzbower, S.R., MacGillavry, H.D., and Blanpied, T.A. (2016). A trans-synaptic nanocolumn aligns neurotransmitter release to receptors. Nature *536*, 210–214.
31. Chazeau, A., Mehidi, A., Nair, D., Gautier, J.J., Leduc, C., Chamma, I., Kage, F., Kechkar, A., Thoumine, O., Rottner, K., et al. (2014). Nanoscale segregation of actin nucleation and elongation factors determines dendritic spine protrusion. EMBO J. *33*, 2745–2764.
32. Pipathsouk, A., Brunetti, R.M., Town, J.P., Graziano, B.R., Breuer, A., Pellett, P.A., Marchuk, K., Tran, N.-H.T., Krummel, M.F., Stamou, D., and Weiner, O.D. (2021). The WAVE complex associates with sites of saddle membrane curvature. J. Cell Biol. *220*, e202003086.
33. Mehidi, A., Kage, F., Karatas, Z., Cercy, M., Schaks, M., Polesskaya, A., Sainlos, M., Gautreau, A.M., Rossier, O., Rottner, K., and Giannone, G. (2021). Forces generated by lamellipodial actin filament elongation regulate the WAVE complex during cell migration. Nat. Cell Biol. *23*, 1148–1162.
34. Huang, Z., Hu, J., Pan, J., Wang, Y., Hu, G., Zhou, J., Mei, L., and Xiong, W.C. (2016). YAP stabilizes SMAD1 and promotes BMP2-induced neocortical astrocytic differentiation. Development *143*, 2398–2409.
35. O'Leary, C.J., Nourse, C.C., Lee, N.K., White, A., Langford, M., Sempert, K., Cole, S.J., and Cooper, H.M. (2017). Neogenin recruitment of the WAVE Regulatory Complex to ependymal and radial progenitor adherens junctions prevents hydrocephalus. Cell Rep. *20*, 370–383.
36. Huang, Z., and Xiong, W.C. (2016). Neogenin-YAP signaling in neocortical astrocytic differentiation. Neurogenesis *3*, e1248735.
37. O'Leary, C.J., Bradford, D., Chen, M., White, A., Blackmore, D.G., and Cooper, H.M. (2015). The Netrin/RGM receptor, Neogenin, controls adult neurogenesis by promoting neuroblast migration and cell cycle exit. Stem Cell. *33*, 503–514.
38. Rajagopalan, S., Deitinghoff, L., Davis, D., Conrad, S., Skutella, T., Chedotal, A., Mueller, B.K., and Strittmatter, S.M. (2004). Neogenin mediates the action of repulsive guidance molecule. Nat. Cell Biol. *6*, 756–762.
39. Tassew, N.G., Charish, J., Seidah, N.G., and Monnier, P.P. (2012). SKI-1 and Furin generate multiple RGMa fragments that regulate axonal growth. Dev. Cell *22*, 391–402.
40. van Erp, S., van den Heuvel, D.M.A., Fujita, Y., Robinson, R.A., Hellemons, A.J.C.G.M., Adolfs, Y., Van Battum, E.Y., Blokhuis, A.M., Kuijpers, M., Demmers, J.A.A., et al. (2015). Lrig2 negatively regulates ectodomain shedding of axon guidance receptors by ADAM proteases. Dev. Cell *35*, 537–552.
41. Sun, X.-D., Chen, W.-B., Sun, D., Huang, J., Li, Y.-Q., Pan, J.-X., Wang, Y.-N., Zhao, K., Dong, Z.-Q., Wang, H.-S., et al. (2018). Neogenin in amygdala for neuronal activity and information processing. J. Neurosci. *38*, 9600–9613.
42. Liakath-Ali, K., Polepalli, J.S., Lee, S.J., Cloutier, J.F., and Südhof, T.C. (2022). Transsynaptic cerebellin 4-neogenin 1 signaling mediates LTP in the mouse dentate gyrus. Proc. Natl. Acad. Sci. USA *119*, e2123421119.
43. Sempert, K., Shohayeb, B., Lanoue, V., O'Brien, E.A., Flores, C., and Cooper, H.M. (2023). RGMa and Neogenin control dendritic spine morphogenesis via WAVE Regulatory Complex-mediated actin remodeling. Front. Mol. Neurosci. *16*, 1253801.
44. Broadhead, M.J., Horrocks, M.H., Zhu, F., Muresan, L., Benavides-Piccione, R., DeFelipe, J., Fricker, D., Kopanitsa, M.V., Duncan, R.R., Klenerman, D., et al. (2016). PSD95 nanoclusters are postsynaptic building blocks in hippocampus circuits. Sci. Rep. *6*, 24626.
45. Nair, D., Hosy, E., Petersen, J.D., Constals, A., Giannone, G., Choquet, D., and Sibarita, J.B. (2013). Super-resolution imaging reveals that AMPA receptors inside synapses are dynamically organized in nanodomains regulated by PSD95. J. Neurosci. *33*, 13204–13224.
46. Lee, N.K., Fok, K.W., White, A., Wilson, N.H., O'Leary, C.J., Cox, H.L., Michael, M., Yap, A.S., and Cooper, H.M. (2016). Neogenin recruitment of the WAVE Regulatory Complex maintains adherens junction stability and tension. Nat. Commun. *7*, 11082.
47. Manley, S., Gillette, J.M., Patterson, G.H., Shroff, H., Hess, H.F., Betzig, E., and Lippincott-Schwartz, J. (2008). High-density mapping of single-molecule trajectories with photoactivated localization microscopy. Nat. Methods *5*, 155–157.
48. Lohmann, C., and Bonhoeffer, T. (2008). A role for local calcium signaling in rapid synaptic partner selection by dendritic filopodia. Neuron *59*, 253–260.
49. Ziv, N.E., and Smith, S.J. (1996). Evidence for a role of dendritic filopodia in synaptogenesis and spine formation. Neuron *17*, 91–102.
50. Yuste, R. (2013). Electrical compartmentalization in dendritic spines. Annu. Rev. Neurosci. *36*, 429–449.
51. Constals, A., Penn, A.C., Compans, B., Toulmé, E., Phillipat, A., Marais, S., Retailleau, N., Hafner, A.S., Coussen, F., Hosy, E., and Choquet, D. (2015). Glutamate-induced AMPA receptor desensitization increases their mobility and modulates short-term plasticity through unbinding from Stargazin. Neuron *85*, 787–803.
52. Wallis, T.P., Jiang, A., Young, K., Hou, H., Kudo, K., McCann, A.J., Durisic, N., Joensuu, M., Oelz, D., Nguyen, H., et al. (2023). Super-resolved trajectory-derived nanoclustering analysis using spatiotemporal indexing. Nat. Commun. *14*, 3353.
53. Koskinen, M., and Hotulainen, P. (2014). Measuring F-actin properties in dendritic spines. Front. Neuroanat. *8*, 74.
54. Borovac, J., Bosch, M., and Okamoto, K. (2018). Regulation of actin dynamics during structural plasticity of dendritic spines: Signaling messengers and actin-binding proteins. Mol. Cell. Neurosci. *91*, 122–130.
55. Chazeau, A., and Giannone, G. (2016). Organization and dynamics of the actin cytoskeleton during dendritic spine morphological remodeling. Cell. Mol. Life Sci. *73*, 3053–3073.
56. Kerruth, S., Coates, C., Dürst, C.D., Oertner, T.G., and Török, K. (2019). The kinetic mechanisms of fast-decay red-fluorescent genetically encoded calcium indicators. J. Biol. Chem. *294*, 3934–3946.
57. Haas, K.T., Compans, B., Letellier, M., Bartol, T.M., Grillo-Bosch, D., Sejnowski, T.J., Sainlos, M., Choquet, D., Thoumine, O., and Hosy, E. (2018). Pre-post synaptic alignment through neuroligin-1 tunes synaptic transmission efficiency. Elife *7*, e31755.
58. Maynard, S.A., Ranft, J., and Triller, A. (2023). Quantifying postsynaptic receptor dynamics: insights into synaptic function. Nat. Rev. Neurosci. *24*, 4–22.
59. Hedrick, N.G., Harward, S.C., Hall, C.E., Murakoshi, H., McNamara, J.O., and Yasuda, R. (2016). Rho GTPase complementation underlies BDNF- dependent homo- and heterosynaptic plasticity. Nature *538*, 104–108.
60. Rottner, K., Stradal, T.E.B., and Chen, B. (2021). WAVE regulatory complex. Curr. Biol. *31*, R512–R517.
61. Sun, D., Sun, X.-D., Zhao, L., Lee, D.-H., Hu, J.-X., Tang, F.-L., Pan, J.-X., Mei, L., Zhu, X.-J., and Xiong, W.-C. (2018). Neogenin, a regulator of adult hippocampal neurogenesis, prevents depressive-like behavior. Cell Death Dis. *9*, 8.
62. Chamma, I., Letellier, M., Butler, C., Tessier, B., Lim, K.H., Gauthereau, I., Choquet, D., Sibarita, J.B., Park, S., Sainlos, M., and Thoumine, O. (2016). Mapping the dynamics and nanoscale organization of synaptic adhesion proteins using monomeric streptavidin. Nat. Commun. *7*, 10773.
63. Lloyd, B.A., Han, Y., Roth, R., Zhang, B., and Aoto, J. (2023). Neurexin-3 subsynaptic densities are spatially distinct from Neurexin-1 and essential for excitatory synapse nanoscale organization in the hippocampus. Nat. Commun. *14*, 4706.
64. Xing, G., Li, M., Sun, Y., Rui, M., Zhuang, Y., Lv, H., Han, J., Jia, Z., and Xie, W. (2018). Neurexin-Neuroligin 1 regulates synaptic morphology and functions via the WAVE regulatory complex in Drosophila neuromuscular junction. Elife *7*, e30457.
65. Lanoue, V., Langford, M., White, A., Sempert, K., Fogg, L., and Cooper, H.M. (2017). The Wnt receptor Ryk is a negative regulator of mammalian dendrite morphogenesis. Sci. Rep. *7*, 5965.
66. Matsuda, T., and Cepko, C.L. (2004). Electroporation and RNA interference in the rodent retina in vivo and in vitro. Proc. Natl. Acad. Sci. USA *101*, 16–22.
67. Rodriguez, A., Ehlenberger, D.B., Dickstein, D.L., Hof, P.R., and Wearne, S.L. (2008). Automated three-dimensional detection and shape classification of dendritic spines from fluorescence microscopy images. PLoS One *3*, e1997.
68. Ojeda, V., Robles-Valero, J., Barreira, M., and Bustelo, X.R. (2015). The disease-linked Glu-26-Lys mutant version of Coronin 1A exhibits pleiotropic and pathway-specific signaling defects. Mol. Biol. Cell *26*, 2895–2912.
69. Kechkar, A., Nair, D., Heilemann, M., Choquet, D., and Sibarita, J.B. (2013). Real-time analysis and visualization for single-molecule based super-resolution microscopy. PLoS One *8*, e62918.
70. Padmanabhan, P., Martínez-Mármol, R., Xia, D., Götz, J., and Meunier, F.A. (2019). Frontotemporal dementia mutant Tau promotes aberrant Fyn nanoclustering in hippocampal dendritic spines. Elife *8*, e45040.

STAR★METHODS

KEY RESOURCES TABLE

REAGENT or RESOURCE	SOURCE	IDENTIFIER
Antibodies		
Actin goat polyclonal antibody, 1:1000 WB	SICGEN	Cat#AB0145-200; RRID: AB_2895355
Alexa 405 conjugated donkey anti-mouse IgG antibody	Thermo Fisher	Cat#A48257; RRID: AB_2884884
Alexa 488 conjugated donkey anti-rabbit IgG antibody	Thermo Fisher	Cat#A21206; RRID: AB_2535792
Alexa 546 conjugated donkey anti-mouse IgG antibody	Thermo Fisher	Cat#A10036; RRID: AB_2534012
Alexa 568 conjugated donkey anti-goat IgG antibody	Thermo Fisher	Cat#A11057; RRID: AB_2534104
Alexa 568 conjugated donkey anti-rabbit IgG antibody	Thermo Fisher	Cat# A10042; RRID: AB_2534017
Alexa 647 conjugated donkey anti-guinea pig IgG antibody	Jackson Labs	Cat# 706-605-148; RRID: AB_2340476
Alexa 647 conjugated donkey anti-rabbit IgG antibody	Thermo Fisher	Cat#A31573; RRID: AB_2536183
Cyfip1 rabbit polyclonal antibody, 1:1000 WB and 1:400 IF	Upstate	Cat#07–531; RRID: AB_390148
IRDye 680RD conjugated donkey anti-goat IgG antibody	LI-COR	Cat#926–68074; RRID: AB_10956736
IRDye 680RD conjugated donkey anti-rabbit IgG antibody	LI-COR	Cat#926–68023; RRID: AB_10706167
IRDye 680LT conjugated goat anti-mouse IgG antibody	LI-COR	Cat#926–68073; RRID: AB_10954442
Map2 rabbit polyclonal antibody, 1:250 for IF	Millipore	Cat# AB5622; RRID: AB_91939
Myc mouse monoclonal antibody clone 9E10, 1:1000 IF	Sigma	Cat#M4439; RRID: AB_439694
Neogenin goat polyclonal antibody, 1:250 WB, IF	R&D Systems	Cat#AF1079; RRID: AB_2151002
Neogenin (C-20) goat polyclonal antibody, 1:250 IF	Santa Cruz	Cat#sc-6536; RRID: AB_2151001
PSD95 (6G6-1C9) mouse polyclonal antibody, 1:600	Abcam	Cat#ab2723; RRID: AB_303248
Tubulin rabbit monoclonal antibody, 1:1000 for WB	Cell Signaling	Cat#2125S; RRID: AB_2619646
vGlut1 guinea pig polyclonal antibody, 1:600 for IF	Chemicon/Sigma	Cat#ab5905; RRID: AB 2301751
WAVE1 mouse monoclonal antibody, 1:400 for IF	Biolegend	Cat#817901; RRID: AB_2564815
Chemicals, peptides, and recombinant proteins		
Brain Derived Neurotrophic Factor (BDNF)	Stem Cell Technologies	Cat#78133
Catalase	Sigma	Cat# C100-50MG
Complete Protease Inhibitor Cocktail tablets, Mini EDTA-free	Roche	Cat#04693159001
Duolink Probe Anti-Rabbit MINUS	Sigma	Cat#DUO92005
Duolink Probe Anti-Mouse PLUS	Sigma	Cat#DUO92001
Duolink Probe Anti-Goat PLUS	Sigma	Cat#DUO92003
Doulink *In Situ* Reagents Orange	Sigma	Cat#DUO92010
Glucose Oxidase	Sigma	Cat#G7141-50KU
Laminin	Invitrogen	Cat#23017-015
Lipofectamine 2000	Invitrogen	Cat#11668-019
L-Glutamine	Invitrogen	Cat#25030081
NuPAGE-gel 4–12% Bis-Tris	Invitrogen	Cat#NP0321BOX
Poly-L-Lysine	Merck	Cat#P2636
Immobilon®-FL PVDF membrane	Millipore	Cat#IPFL00010
ProLong™ Glass Antifade Mountant	ThermoFisher	Cat#P36980
Experimental models: cell lines		
Human: HEK293T cell line	ATCC	Cat# CRL-3216, RRID:CVCL_0063
Mouse: NE-4C cell line	ATCC	Cat#CRL-2925, RRID:CVCL_B063

(*Continued on next page*)

Continued

REAGENT or RESOURCE	SOURCE	IDENTIFIER
Experimental models: organisms/strains		
Mouse: C57BL/6J	University of Queensland Biological Resources	RRID:IMSR_JAX:000664
Oligonucleotides		
shCtl target sequence: 5′ GTCTCCACGCGCAGTACATTT 3′	Sempert et al.[43]	N/A
shNeo target sequence: 5′ CTGAAGCTAACGGCAAGATTA 3′	Sempert et al.[43]	N/A
shCyfip1 target sequence#1: 5′ CCAGATTCTCAACGATGAAA 3′	De Rubeis et al.[24]	N/A
shCyfip1 target sequence#2: 5′ CCAGATTCTCAACGATGAAAT 3′	De Rubeis et al.,[24]	N/A
Recombinant DNA		
pCAG-EmGFP-Ctl shRNA	Sempert et al.[43]	N/A
pCAG-EmGFP-Neo shRNA	Sempert et al.[43]	N/A
pCAG-Cyfip1-mEos3.1+Cyfip1-shRNA#2	This paper	
pCI-*syn*-fRGECO1	Addgene	Cat #125243
pEF-FL-Neo-myc	Sempert et al.[43]	N/A
pEF-FL-NeoΔWIRS-myc	Sempert et al.[43]	N/A
pEF-FL- Neo-mEos3.1	This paper	N/A
pEF-FL-NeoΔWIRS-mEos3.1	This paper	N/A
pRFPRuby-N1-Lifeact	Ojeda et al.[65]	
Software and algorithms		
Fiji	National Institutes of Health	RRID: SCR_002285, https://fiji.sc/
GraphPad Prism 9.4.0	GraphPad	RRID: SCR_002798, https://graphpad.com
Huygens Professional	Scientific Volume Imaging, SVI	RRID: SCR_014237, https://svi.nl/Huygens-Microscopy-Analysis-Software
Imaris 9.9	Oxford Instruments	RRID:SCR_007370, https://imaris.oxinst.com/
MetaMorph, PALM-tracer	Molecular Devices Nair et al.[45]; Kechkar et al.[66]	RRID: SCR_002368, https://www.moleculardevices.com/products/cellular-imaging-systems/acquisition-and-analysis-software/metamorph-microscopy#gref
NASTIC	Wallis et al.[52]	
Neurolucida 360	MBF Bioscience	RRID: SCR_016788, https://www.mbfbioscience.com/products/neurolucida-360
Odyssey Imaging Studio	LI-COR	RRID: SCR_022510, https://www.licor.com/bio/image-studio/
Black Zen software	Zeiss Microscopy	RRID: SCR_018163, https://www.zeiss.com/microscopy/int/products/microscope-software/zen.html

RESOURCES AVAILABILITY

Lead contact

Further information and requests for resources and reagents should be directed to and will be fulfilled by the Lead Contact, Helen Cooper (h.cooper@uq.edu.au).

Materials availability

The plasmids generated in this study can be requested from the lead contact, Helen Cooper (h.cooper@uq.edu.au).

Data and code availability

- Data: The microscopy data and other relevant data reported in this paper will be shared by the lead upon request.
- Code: This paper does not include original code.
- Additional information: Any additional information required to reanalyze the data reported in this paper will be shared by the lead upon request.

EXPERIMENTAL MODEL AND STUDY PARTICIPANTS

Primary hippocampal neuronal cultures were prepared from C57BL/6J embryos at embryonic day 18.5 (Lanoue et al., 2017).[43,65] Briefly, hippocampi were dissected, dissociated with trypsin (Invitrogen) (20 min, 37C) and neutralized with DMEM (Invitrogen) supplemented with 10% (v/v) fetal bovine serum (FBS, Sigma). Dissociated neurons were plated on poly-L-lysine (Merck) and laminin (Invitrogen) coated 12 mm glass coverslips (4.5×10^4 cells/well, 24 well plate), 29 mm glass bottom dishes (Cellvis, 10×10^4 cells/dish) or glass bottom 8-well chamber slides (Ibidi, 2.4×10^4 cells/well). Cultures were maintained in Neurobasal medium (Invitrogen), 2% B27-supplement (Invitrogen) and 0.5 mM L-glutamine (Invitrogen) (37°C, 5% CO_2) with 50% medium replacement every 3 days. All experiments involving animals were approved by the Anatomical Biosciences Animal Ethics Committee of The University of Queensland (project number: 2021/AE000482) and performed in accordance with the Australian Code of Practice for the Care and Use of Animals for Scientific Purposes.

- Human participants were not used in this study.

METHOD DETAILS

Neuronal transfection

Neurons were transfected at DIV12 in Neurobasal medium using Lipofectamine 2000 (Invitrogen) according to the manufacturer's instructions. Neurons were transfected for 1–2 h as follows: 24-well plates, 0.75 μg DNA, 2 μL Lipofectamine 2000/well; 8-well chambers, 0.24 μg DNA, 1 μL Lipofectamine 2000/well; 29 mm glass bottom wells, 1 μg DNA, 1 μL Lipofectamine 2000/dish. Experiments were performed between DIV14-15 post-transfection.

Constructs and shRNAs

Neogenin constructs

Full-length mouse Neogenin (6 × myc epitopes added to the C-terminus) was cloned into pCAGIG which includes an IRES-GFP sequence to visualize neurons.[66] The shRNA resistant mouse Neogenin construct was generated by mutating 4 nucleotides within the shRNA target sequence. For the mutant NeoΔWIRS construct, the WIRS motif amino acids S1314 and F1315 (NCBI: 18007) were mutated to alanine using the QuickChange II XL Site-Directed Mutagenesis Kit (Agilent Technologies).[43,46] For single-particle tracking experiments mEos3.1 was fused in-frame to the Neogenin C-terminus. shRNAs were expressed using the BLOCK-iT RNA-Polymerase II miRNA expression vector system (Thermo Fisher) which co-cistronically expresses Emerald GFP under the control of the CAG-promoter. In these constructs the shRNA sequence is embedded in the 3′ UTR of GFP, ensuring that the shRNAs are co-expressed with GFP. shRNA sequences[43]: shNeo12, TAATCTTGCCGTTAGCTTCAG; shCtl, AAATGTACTGCGCGTGGAGAC.

Cyfip1 constructs

Mouse Cyfip1 (GenBank: NM_011370) was expressed in the BLOCK-iT RNA-Polymerase II miRNA expression vector system where GFP in the 3′ UTR was replaced with Cyfip1-mEos. mEos3.1 was fused in-frame to the C-terminus. The shRNA resistant Cyfip1-mEos construct was generated by introducing 5 silent mutations within the shRNA target sequence: TTcCAgATtCTcAAcGATGAAATC >TTtCAaATaCTgAAtGATGAAATC with no change in amino acid sequence (FQILNDEI). shRNA sequences[24]: shCyfip1#1, CCAGATTCTCAACGATGAAAT; shCyfip1#2, CCAGATTCTCAACGATGAAA.

Analysis of shRNA efficiency

HEK293T cell transfection

Cells were plated in 6-well plates (Costar) at 0.3×10^6 cells/well. On the following day, cells were transfected using Lipofectamine 2000 according to the manufacturer's instructions. A total of 1 μg DNA and 3 μL Lipofectamine 2000/well were mixed in Opti-MEM (Invitrogen) for 20 min and then incubated with cells for 4 h. The medium was then replaced with DMEM (Invitrogen) supplemented with 10% (v/v) FBS for 48 h.

NE-C4 cell transfection

Mouse NE-C4 neuroepithelial cells were plated at 0.2×10^6/well in 6-well plates and transfected using Lipofectamine 2000. A total of 2 μg DNA and 6 μL Lipofectamine 2000/well were mixed in Opti-MEM for 20 min and then incubated with the cells for 24 h. The medium was then replaced with DMEM (10% (v/v) FBS) for 24 h.

Cell lysis and western blotting

Cells were lysed in RIPA buffer [150 mM NaCl (Chem-supply), 50 mM Tris-HCl pH7.5 (Amresco), 0.5% sodium deoxycholate (Sigma), 1% Triton X-100 (Sigma), 0.1% SDS (Amresco), 50 mM NaF (Sigma), 10 mM sodium pyrophosphate (Sigma), 2 mM EDTA (Chem-supply) and 2 mM EGTA (Sigma)] supplemented with Complete Inhibitors (Mini EDTA-free, Roche). Cell lysates were centrifuged at 14 × 10^3 g for 20 min and denatured in 1× Laemmli buffer [200 mM Tris-HCl, 8% (v/v) SDS, 40% (v/v) glycerol (Chem-supply), 0.4% (v/v) bromophenol blue (Sigma), and 100 mM dithiothreitol (Sigma)] to a total volume of 25 μL at 50C. Samples were separated by SDS-PAGE using NuPAGE 4–12% Bis-Tris Protein Gels (Invitrogen) and transferred to Immobilon-FL PVDF membranes (Millipore). After blocking (1 h, Intercept Blocking Buffer, LI-COR), membranes were incubated with primary and secondary antibodies. Proteins were visualized using an Odyssey scanner system including LI-COR scanning software. Densiometric analysis was performed using FIJI (National Institutes of Health, USA).

Immunocytochemistry

Neurons were fixed in 2% paraformaldehyde (20 min), permeabilized with 0.1% Triton X-100 (5 min) and then blocked with 10% FBS, 1% BSA (Sigma) in PBS (1 h, 37C) in a humid chamber. Primary antibodies were incubated overnight in the blocking solution. Following secondary antibody application, neurons were washed and mounted in ProLong Mountant (Thermo Fisher). Primary and secondary antibodies are listed in the key resources table. Confocal images were acquired on a Zeiss LSM 710 confocal microscope (58.67 × 58.67 μm, 0.06 μm/pixel). The colocalization maps were generated in Imaris9.9 (Oxford Instruments) and image analysis performed using the ImageJ plugin from FIJI. Super-resolution confocal images were acquired on a Zeiss LSM 980 NLO Airyscan2 confocal microscope (57.71 × 57.71 μm, 0.035 μm/pixel). The Zeiss LSM is equipped with 32 Airyscan detector elements, where each detector acts as a small pinhole and gathers extra light, thereby providing further resolution of 120 nm. Subsequent joint deconvolution allows up to 90 nm separation.

Spine analysis

GFP-positive neurons were randomly selected, and z-stacks (z-step size 110 nm) obtained using a Nikon Plan Apochromat 100×/1.45 NA oil-immersion objective on a spinning disk confocal microscope (Diskovery, Andor Technology/Nikon Ti-E microscope body). The acquired images (150 × 80 μm, 0.054 μm/pixel) were processed by deconvolution using Huygens Professional (Scientific Volume Imaging). Tracing was performed using Neurolucida 360 (MBF Bioscience) on secondary and tertiary dendrites where 1–2 dendrites/neuron (9 neurons/condition) were traced using the smart manual tracing mode.[43] The total length of traced secondary and tertiary dendrites was 300–400 μm and the last 20 μm of the dendrite were excluded from the analysis. The proportion of mushroom spines was expressed as a percentage of mushroom, stubby, thin spines and filopodia per neuron pooled across 9 neurons/condition from 3 independent experiments. Spines was automatically detected using the following Neurolucida parameter set[43]: outer range, 7.5 μm; minimum height, 0.3 μm; detector sensitivity, 150; minimum count, 35. Spines were classified using the following parameter set: head-to-neck ratio, 1:1.2; length-to-head ratio 1:2.5; head size 0.6 μm; filopodium length 3.5 μm.[43,67]

BDNF stimulation

In all experiments, neurons were incubated with BDNF (65 ng/mL) for 1 h before live-imaging or fixation with 2.5% PFA with the exception of the calcium imaging study where imaging commenced prior to treatment.

Proximity ligation assay

Quantification of Neogenin-Cyfip1 interactions was carried out using the Duolink Proximity Ligation Assay (Sigma) according to the manufacturer's instructions. Images were captured using a Zeiss LSM 710 confocal microscope (58.67 × 58.67 μm, 0.06 μm/pixel) and the extent of interaction was calculated by quantifying the number of spines associated with fluorescent puncta using the ImageJ Cell Counter plugin. The number of puncta-positive spines was expressed as a percentage of total spines along a 50 μm segment of secondary or tertiary dendrites (15–20 neurons, 15–20 spines/neuron) from 3 independent experiments. For the experiment in Figure S2C, neurons were first cotransfected with GFP and Neogenin (Neo-myc) (6 × myc epitopes added to the C-terminus) or NeoΔWIRS-myc[46] and the PLA performed with anti-myc and anti-Cyfip1 antibodies. For experiment in Figure S7, neurons were treated with 65 ng/mL BDNF for 1h before fixation.

Fluorescence recovery after photo bleaching

Neurons were cultured on 29 mm dishes (Cellvis, 10 × 10^4 cells/dish) and cotransfected with RFP-Lifeact[68] with either shCtl or shNeo and *Neo* or NeoΔWIRS. FRAP was performed on live neurons 65 ng/mL BDNF (60 min, Miltenyi Biotec) and images collected on the Zeiss LMS 710 confocal microscope using a 63×/1.4 NA oil-immersion objective (71 × 71 μm, 0.069 μm/pixel). Regions of interest (ROIs, 8.5 ± 0.3 μm^2 equivalent to the spine diameter) were selected over the mushroom spine and the background and reference ROIs were set elsewhere on the same neuron using the FRAP module of the Black Zen software. To achieve sufficient bleaching 100% laser power at 405 nm and 561 nm was used at the ROIs after frame 10 for 20 iterations at 1.93 s intervals and images acquired every 1.93 s for 200 s. The Black Zen FRAP module was then used to subtract the background fluorescence, normalize the data against the unbleached reference ROI and to calculate the stable fraction.[53] 15–16 BDNF-treated neurons and 8–9 BDNF-untreated neurons were analyzed from 3 independent experiments. 3–6 mushroom spines on secondary dendrites were analyzed and averaged per neuron.

Calcium imaging

Neurons cultured in glass bottom 8-well chamber slides (Ibidi, 2.4 × 10^4 cells/well) were cotransfected with fRGECO1 (pCI-*syn*-fRGECO1 was a gift from Katalin Torok,[56] (Addgene plasmid #125245) and either shCtl or shNeo and rescued with *Neo* or NeoΔWIRS. At DIV14, a random neuron per well was selected and calcium levels were assessed following the addition of BDNF (65 ng/mL) 25 s after the start of imaging. Neurons were imaged in phenol red free medium (125 mM NaCl, 2.5 mM KCl, 25 mM HEPES pH7.4, 33 mM glucose, 1 mM $MgCl_2$) using a Marianas TIRF microscope equipped with a Quant EM X2 CCD camera and frames were captured at 40 ms/frame for 2000 frames with the intensification set at 900 using a TERF 100× oil-immersion objective (77.26 × 77.26 μm, 0.302 μm/pixel) controlled by Slidebook 6 software. The relative fluorescence intensity (ΔF/F0) was calculated using ImageJ as follows; baseline fluorescence intensity (F0) was determined 5 s prior to BDNF treatment and the change in fluorescence after the addition of BDNF (ΔF) was calculated by subtracting F0 from the intensity observed in subsequent frames (F). ΔF/F0 per neuron was obtained by averaging the ΔF/F0 values of 3–6 mushroom spines along 50 μm of secondary dendrites. 11–15 neurons were imaged/condition from 3 independent experiments. The ROUT outlier statistical test was used to exclude outlier neurons.

Stochastic optical reconstruction microscopy (STORM)

Neurons were cultured on glass bottom 29 mm dishes and transfected with pCAG tdTomato. Immunostaining was performed as described above using goat anti-C-terminal Neogenin (1:250; C-20, Santa Cruz) and rabbit anti-Cyfip1 (1:400; Upstate). The secondary antibodies (donkey anti-goat Alexa 647, donkey anti-rabbit Alexa 488, 1:600) were incubated for 1 h followed by thorough washing. STORM imaging was performed using an Abbelight SAFe 360 single-molecule localization microscope (imaging buffer: 1× PBS, 10% glucose, 0.6 mg/mL glucose oxidase, 100 mM mercaptoethylamine and 60 μg/mL catalase; pH7.5–8.5). Cells were initially bleached with 100% laser power at 488 nm and 640 nm. STORM acquisition was then initiated at a TIRF angle of 66 with 40 ms intervals between streaming frames for 5000 frames using a CFI Apo TIRF 100xC/1.49 NA oil-immersion objective (59.75 × 59.75 μm, 97 nm/pixel). The localization precision of the 488 nm and 639 nm lasers used to excite the Alexa Fluor 647 and 488 dyes on the Abbelight SAFe 360 scope allows a resolution of 15 nm. The localization accuracy averaged from 600 detections is 22.25 nm ± 19.13 StD for Alexa Fluor 488 and 26.19 nm ± 22.34 StD for Alexa Fluor 647.

Acquired STORM videos were processed in Abbelight *NEO* software. Parameters used for localizing detections using Gaussian fitting-LSQ: minimum PSF area; 9 pixels, maximum PSF area; 50 pixels, local mean kernel size; 15 pixels. In reconstructed STORM images pixel resolution was 15 nm/pixel. To quantify Cyfip1 and Neogenin association and spine size Abbelight NEO-generated images of super-resolved detections were analyzed in ImageJ. 50–70 mushroom spines were analyzed on secondary dendrites of 8 neurons from 3 independent experiments. A threshold of 100 nm diameter was used to calculate the Neogenin large to small cluster ratio.

Single-particle tracking using photoactivation localization microscopy (sptPALM)

Neurons (DIV14-15) were imaged in phenol red free medium. Live movies were acquired on a Roper iLas 2 microscope (Roper Scientific) using a Nikon CFI Apo TIRF 100×/1.49 NA oil-immersion objective (Nikon Instrument) which allows long-term oblique illumination allowing resolution of 20–25 nm. The microscope was equipped with an Evolve512 Delta EMCCD camera (Photometrics), Piezo Z-drive and Nikon perfect focus system. To exclude autofluorescence and background noise, a dichroic beamsplitter (LF488/561-A-000, Semrock) and double emission filters (FF01-523/610-25, Semrock) were used. Metamorph software (version 7.7.8, Molecular Devices) was used to control image acquisition. Time-lapse movies of the ROI (250 × 400 pixels, 106 nm/pixel, 37C, 5% CO_2) were captured over 25,000 frames (20 ms exposure/frame, 50 frames/s, 50 Hz). For sptPALM, 405 nm at 2% laser power was used to photoswitch mEos. Simultaneously, 70% 561 nm laser power was used to excite and bleach the photoconverted mEos. Neurons were imaged before the addition of BDNF and 1 h after treatment with 65 ng/mL BDNF.

Single-particle tracking analysis was performed using PALM-tracer in MetaMorph software.[45,69] The mean squared displacement was determined as a function of time for each trajectory which was individually tracked over a minimum of 8 frames. For each trajectory the mobility threshold was set at 3 pixels with 318 nm between consecutive frames. The diffusion coefficient was calculated from the slope of the mean squared displacement (MSD) versus time curve according to the equation MSD(t) = a + 4Dt, where D is the diffusion coefficient, a = *y*-intercept and t = time. The diffusion coefficient threshold was defined using the following equation: $Log_{10}[D_{threshold}$= (spatial resolution)^2/(4 × 4 x temporal resolution)].[51,70] The following values were used: spatial resolution = 0.106 μm, temporal resolution = 0.02 s). Trajectories with $Log_{10} \leq -1.45$ μm^2/s were considered immobile. For statistical comparison, immobile and mobile fractions were calculated from the frequency distribution curve of the diffusion coefficient. 10–15 mushroom spines on 50 μm secondary dendrites and a total of 13–16 neurons were analyzed per condition from 3 independent experiments. Nanocluster behavior was determined using NASTIC[52] after setting the following parameters: minimum trajectory length, 8 frames; maximum trajectory length, 100 frames; frame time, 0.02 s; radius factor, 1.2; minimum trajectory overlap/cluster, 3 trajectories); Neo cluster size radius, 0.15 μm and Cyfip1 cluster size radius, 0.20 μm.

QUANTIFICATION AND STATISTICAL ANALYSIS

All imaging experiments were performed on mushroom spines. Statistical analyses were performed using GraphPad Prism (GraphPad 9.4.0). All experimental data were derived from a minimum of 3 independent biological replicates and tested for normality (Gaussian distribution) using the Kolmogorov-Smirnov test. Statistical significance was then determined using an unpaired Student's t test for two group comparisons. One or two-way ANOVA followed by Tukey's multiple comparisons *post hoc* test was used to compare three or more groups when data were normally distributed. Non-parametric data (Figures 5D–5F and 7D–7F) were transformed using sqrt(x+1) to reach normality after which two-way ANOVA was applied followed by Tukey's *post hoc* test. All values are presented as mean ± standard error of the mean (SEM). Statistical significance was considered to be $p < 0.05$.